Multiomic single-cell lineage tracing to dissect fate-specific gene regulatory programs

Kunal Jindal[1,2,3], Mohd Tayyab Adil[1,2,3], Naoto Yamaguchi[1,2,3], Helen C. Wang[4], Xue Yang[1,2,3], Kenji Kamimoto[1,2,3], Guillermo C. Rivera-Gonzalez[1,2,3], and Samantha A. Morris[1,2,3].

[1]Department of Developmental Biology; [2]Department of Genetics; [3]Center of Regenerative Medicine. [4]Department of Pediatrics, Division of Hematology and Oncology, Washington University School of Medicine, 660 S. Euclid Avenue, St. Louis, MO 63110, USA. *Correspondence: s.morris@wustl.edu

Abstract

Complex gene regulatory mechanisms underlie differentiation and reprogramming. Contemporary single-cell lineage tracing (scLT) methods use expressed, heritable DNA barcodes to combine cell lineage readout with single-cell transcriptomics enabling high-resolution analysis of cell states while preserving lineage relationships. However, reliance on transcriptional profiling limits their adaptation to an ever-expanding tool kit of multiomic single-cell assays. With CellTag-multi, we present a novel approach for profiling lineage barcodes with single-cell chromatin accessibility without relying on co-assay of transcriptional state, paving the way for truly multiomic lineage tracing. We validate CellTag-multi in mouse hematopoiesis, characterizing transcriptional and epigenomic lineage priming across progenitor cell populations. In direct reprogramming of fibroblasts to endoderm progenitors, we use CellTag-multi to comprehensively link early cell state with reprogramming outcomes, identifying core regulatory programs underlying on-target and off-target reprogramming. Further, we reveal the Transcription Factor (TF) Zfp281 as a novel regulator of reprogramming outcome, biasing cells towards an off-target mesenchymal fate via its regulation of TGF-β signaling. Together, these results establish CellTag-multi as a novel lineage tracing method compatible with multiple single-cell modalities and demonstrate its utility in revealing fate-specifying gene regulatory changes across diverse paradigms of differentiation and reprogramming.

Keywords: Single-cell lineage tracing; Transcriptomics; Chromatin accessibility; Epigenomics; Multiomics; Hematopoiesis; Reprogramming.

Introduction

The quantification of cell identity is crucial to understanding development, disease, and homeostasis, yet the notion of cell identity remains poorly defined[1]. Single-cell technologies, now tailored to diverse modalities[2], are expanding our understanding of how cell identity is established and maintained[3]. In particular, single-cell lineage tracing (scLT) methods allow cell relationships to be tracked throughout biological processes, revealing cell fate decisions during differentiation and reprogramming[4,5]. A suite of scLT tools are based on labeling cells with unique genetic 'barcodes' that are expressed as RNA; capturing these barcodes via single-cell RNA-seq (scRNA-seq) has allowed the parallel capture of lineage information and single-cell transcriptomes[6–13].

Virus-based methods to barcode and track cells have been deployed across several *in vitro* differentiation and reprogramming paradigms[5,14]. The accessibility of cells within these systems permits longitudinal sampling, allowing early progenitor state to be linked to terminal fate (termed 'state-fate analysis'; **Fig. 1a**). Such a strategy has been used to determine how well gene expression state in progenitors reflects eventual cell fate in hematopoiesis[13]. This work demonstrated that subsequent fate could be predicted, albeit with limited accuracy, from progenitor gene expression, indicating the existence of heritable fate determinants that are not captured by scRNA-seq alone. Similarly, viral barcoding, 'CellTagging,' of transcription factor-mediated direct reprogramming of mouse embryonic fibroblasts (MEFs) to induced endoderm progenitors (iEPs), suggested that reprogramming outcome is determined during the early stages of fate conversion[7]. However, the early gene regulatory changes that set cells on their destined path have not been fully characterized. Additional information from epigenomic assays such as single-cell Assay of Transposase Accessible Chromatin by sequencing (scATAC-seq) may be crucial to uncover the heritable properties that play a key role in the establishment and maintenance of cell identity.

To adapt scLT for chromatin accessibility capture, we have developed 'CellTag-multi.' CellTag-multi is based on our previous CellTagging technology, which uses sequential lentiviral delivery of CellTags (heritable random barcodes) to enable the construction of multi-level lineage trees[7,15]. Here, we introduce a new strategy in which CellTags are expressed as polyadenylated transcripts, which can be captured in adapted scRNA-seq and scATAC-seq library preparation. Cells are transduced with this modified complex lentivirus library, resulting in their unique labeling with heritable barcode signatures and simultaneous tracking of clonal transcriptional and epigenomic state.

We validate this method using *in vitro* hematopoiesis, a well-characterized model of multi-lineage differentiation, and demonstrate high fidelity capture of lineage-specific chromatin state and gene expression priming across progenitors. Moreover, the addition of chromatin accessibility

68 information to gene expression allows for a significant improvement in the prediction of
69 differentiation outcome from early progenitor state. We also deploy CellTag-multi in the direct
70 lineage reprogramming of fibroblasts to induced endoderm progenitors (iEPs), to characterize
71 early genomic events in rare subpopulations of cells that successfully reprogram. This application
72 reveals how chromatin is remodeled following expression of reprogramming TFs, enabling deeper
73 insight into gene regulatory network reconfiguration. We uncover the TF Foxd2 as a facilitator of
74 on-target reprogramming, increasing the efficiency of MEF to iEP conversion. Conversely, we
75 identify Zfp281 as a TF biasing cells towards an off-target mesenchymal fate via its regulation of
76 TGF-β signaling, which we validate experimentally. We demonstrate that the identification of
77 these TFs as novel reprogramming regulators is only possible via multiomic profiling. Together,
78 these findings highlight the utility of CellTag-multi in defining the molecular regulation of early cell
79 state and its relation to fate across diverse biological applications.
80
81 **Development and validation of CellTag-multi**
82 CellTagging relies on single-cell capture of CellTags — heritable DNA barcodes expressed as
83 polyadenylated transcripts[7,15,16]. In the standard workflow, CellTags are captured as transcripts
84 and reverse transcribed (RT), along with cellular mRNA, during 3' end scRNA-seq library
85 preparation. In contrast, scATAC-seq directly captures fragments of the accessible genome,
86 omitting capture of CellTag transcripts, rendering CellTagging incompatible with scATAC-seq
87 assays. To enable CellTag profiling with scATAC-seq, we introduced two essential modifications.
88 First, we developed an *in situ* Reverse Transcription (isRT) step to selectively reverse transcribe
89 CellTag barcodes inside intact nuclei. By introducing this additional step after transposition, we
90 omitted the need to RT CellTags during scATAC-seq library construction. Second, we modified
91 the CellTag construct to flank the random barcode with Nextera Read 1 and Read 2 adapters
92 (**Fig. 1b, Ext Fig. 1a, b**).
93 During scATAC-seq library preparation, nuclei are partitioned into nanoliter droplets along
94 with single-cell barcoding beads and PCR reagents. Each bead contains a barcoded forward
95 primer complementary to the Nextera Read 1 adapter to barcode and linearly amplify all ATAC
96 fragments during the GEM incubation step. By inserting Nextera Read 1 and Read 2 adapters in
97 the CellTag construct, we enabled single-cell capture of reverse transcribed CellTags along with
98 accessible chromatin during the GEM incubation stage (**Fig. 1c, Ext Fig. 1b**). This strategy
99 improved the CellTag capture rate by >200-fold compared to the unmodified scATAC-seq protocol
100 (**Ext Fig. 1c**). Additionally, we introduced a reverse primer specific to the CellTag cDNA during
101 GEM incubation to exponentially amplify CellTag fragments, while ATAC fragments undergo

linear amplification (**Supplementary Table 1, Ext Fig. 1b**). Together, these modifications led to a >50,000-fold increase in CellTag capture (**Ext Fig. 1c**), with CellTags being detected in >96% of cells in scATAC-seq relative to 98% in scRNA-seq (**Ext Fig. 1d**), without negatively impacting scATAC-seq data quality or genome-wide chromatin accessibility signal (**Fig. 1d, e, Ext Fig. 1e, f**).

To support the accurate identification of clonally related cells, it is essential that CellTag signatures from individual cells are captured with high fidelity, minimizing background noise. To assess the fidelity of CellTag signatures captured in scATAC-seq, we performed a species-mixing experiment (**Ext Fig. 2a**). We labeled human (HEK 293T) cells and mouse (expanded iEPs) cells with two different versions of the CellTag-multi library, combined nuclei isolated from both populations in a 1:1 ratio and profiled them using our modified scATAC-seq method. Plotting CellTag reads/cell, we observed that nuclei from each species predominantly consisted of reads from the expected CellTag library, indicating minimal inter-species crosstalk (**Fig. 1f; Ext Fig. 2b, c**).

Finally, to perform large-scale lineage tracing experiments, we synthesized a complex CellTag-multi library containing ~80,000 unique barcodes, as confirmed by sequencing (**Supplementary Table 2**, **Methods**). We applied CellTag-multi to a population of expanded mouse fibroblasts undergoing reprogramming to iEPs and profiled clones with scRNA-seq and scATAC-seq, detecting CellTags in 70% (RNA) and 51% (ATAC) of the cells at an average MOI of 2 (RNA) and 2.5 (ATAC). Filtering, error-correction, and allowlisting of CellTag reads (**Methods**) enabled high-fidelity identification of distinct clones across the two single-cell modalities (**Fig. 1g, h, Ext Fig. 2d-f**). As expected, the correlation between gene expression and accessibility was higher within clones than across clones (**Fig. 1i, j**). These analyses established the efficacy of CellTag-multi for the labeling and capture of clonally related cells across scRNA and scATAC modalities. Next, we leveraged CellTag-multi to link early state with cell fate in diverse cell fate specification and reprogramming paradigms.

Benchmarking CellTag-multi using an *in vitro* model of mouse hematopoiesis

To validate lineage analysis across single-cell modalities with CellTag-multi, we applied it to hematopoiesis, a well-characterized paradigm for multi-lineage differentiation. Recently, scLT was used to define the early transcriptional cell states that lead to defined differentiation outcomes in mouse hematopoiesis. However, these analyses suggested that early transcriptional changes alone cannot fully define future cell fate and posited a role for cell states that evade transcriptional profiling, collectively termed hidden state variables[13]. In this context, we aimed to apply CellTag-

multi to further refine state-fate linkages in early hematopoiesis by identifying fate-specific changes in both early gene expression and chromatin accessibility.

We isolated Lin$^-$, Sca1$^+$, c-Kit$^+$ (LSK) cells from adult mouse bone marrow and cultured them in broad myeloid differentiation media[13]. Upon isolation, we tagged these cells with the CellTag-multi library to track clones across modalities. To capture both early state and fate across clones, we profiled half of the cells 60 hours after initiation of differentiation (Day 2.5; state sample), re-plated the remaining cells across two technical replicates, and collected them for sequencing on Day 5 (fate sample). In the case of both samples, cells were split between scRNA-seq and scATAC-seq (**Fig. 2a**), resulting in the profiling of 9,789 state cells (scRNA-seq: n=5,161; scATAC-seq: n=4,628) and 67,029 fate cells (scRNA-seq: n=56,534; scATAC-seq: n=10,495 cells), after quality filtering (**Ext Fig. 3a, b**). CellTagging was consistent across single-cell modalities, yielding 83-99% labeled cells. We identified 37,441 scRNA-seq cells in 5,973 clones and 6,098 scATAC-seq cells in 3,012 clones, labeled with 4.2 CellTags/cell (in scRNA-seq) and 3.4 CellTags/cell (in scATAC-seq) on average (**Ext Fig. 3c**). 2,227 clones spanned both state and fate samples, including 877 multiomic clones (**Ext Fig. 3d**).

For visualization, we co-embedded cells from both modalities using Canonical Correlation Analysis (CCA)[17]. Further, we devised a unique clone-cell co-embedding approach to include clones as individual data points in a single-cell embedding, enabling straightforward visualization and assessment of clone-level metadata and global trends across clones (**Fig. 2b**). We first extracted the cell-cell similarity graph, produced as part of standard single-cell analysis workflows. In this graph, each cell is represented by a node and the connection between a pair of cells is weighted based on their phenotypic similarity. Next, we imputed abstract clone nodes and clone-cell edges to this graph based on clonal data. Finally, we used this expanded clone-cell graph as input for dimensionality reduction algorithms such as UMAP[18] or ForceAtlas[19] to produce a single 2D-embedding of the data, where both cells and clones are represented by individual points. We applied this visualization to the hematopoiesis data to co-embed RNA and ATAC cells with all clones, with minimal impact on the underlying structure of the data (**Fig. 2c, Ext. Fig. 3e, f**). Clones, now represented as individual data points, faithfully represented their constituent cells (**Ext Fig. 3g**) and can be used to visualize clonal metadata across all cells (**Fig. 2c, right panel**). We annotated cells using marker gene expression and Seurat[17] label transfer, recapitulating continuous transitions from immature progenitor cells toward several differentiated hematopoietic lineages across single-cell modalities as previously reported[13,20,21] (**Fig. 2c middle panel, Ext Fig. 3h-j**). While CellTag capture was uniform across cell states (**Ext Fig. 4a, b**), we observed

169 higher clonal expansion along the monocyte lineage, consistent with our myeloid differentiation
170 culture conditions (**Fig. 2c right panel, d**).
171 To link Day 2.5 cell state with Day 5 fate, we assigned each clone a fate label based on
172 the most abundant cell type amongst its Day 5 sisters (**Fig. 2e**, **Ext Fig. 4c**). We mapped early
173 clonal state along the differentiation continuum, extending our clone-cell embedding approach
174 further and splitting each clone into sub-clones (up to four) based on the assay and time point
175 capture of each sister (**Ext Fig. 4d**). While Day 5 fate sub-clones localized largely within their
176 respective cell fate clusters (**Ext Fig. 4e**), Day 2.5 state sub-clones associated with each major
177 fate formed distinct groups closer to the undifferentiated progenitors (**Fig. 2f, g**), suggesting early
178 functional priming of immature cells. Moreover, state sub-clones within the same 'fate potential'
179 group overlapped significantly across single-cell modalities (Mann Whitney Wilcoxon test; p-value
180 = 3.76e-5, **Fig. 2g, h**), demonstrating high-fidelity capture of state-fate linkages across
181 transcriptional and epigenomic states with CellTag-multi. Projecting fate bias scores, defined as
182 the fraction of fate sisters belonging to the assigned clonal fate, on to state sub-clones, we
183 observed that low fate bias clones occupied areas closer to the overlapping boundaries of each
184 fate potential region, likely indicating areas of multi-potency (**Fig. 2g, Ext Fig. 4f**).
185 To characterize these fate-specific changes in early cell state on a molecular level, we
186 assessed the enrichment of transcriptional and epigenetic signatures in Day 2.5 sisters for each
187 fate group (**Fig. 2i; Methods**). Using gene expression, we identified several known fate-specific
188 markers in each group, such as *Spp1*[13] and *Ms4a3*[22] in the Monocyte primed group; *Elane* and
189 *Ctsg*[13] in the Neutrophil primed group; *Pf4*[23] and *Gata2*[13] in the Erythroid/Megakaryocyte groups.
190 In the Lymphoid group, we identified *Flt3*, a predominantly Lympho-myeloid gene[24], and several
191 lymphoid fate-specific genes such as *Mef2c*[25] and *Bcl11a*[26]. For epigenetic data, we focused on
192 TF activity scores[27], which estimate the enrichment of TF motifs in single-cell epigenomes[27].
193 Unlike peak accessibility, TF activity feature space is dense and continuous, allowing comparison
194 between small groups of cells, and is easier to interpret relative to individual peak features[27]. TF
195 activity enrichment analysis revealed several expected lineage specifying TFs for each fate[20,28],
196 such as several CEBP TFs enriched in Monocyte and Neutrophil primed groups; GATA1 and
197 GATA2 in the Erythroid/Megakaryocyte and Basophils/Eosinophils/Mast cells groups; Lympho-
198 myeloid TF SFPI1 (also known as PU.1) in the Lymphoid and Dendritic Cells (DC) group, along
199 with BCL factors and MEF2 factors, indicating extensive epigenomic priming in early cells towards
200 their respective cell fate. A complete list of differential gene expression and TF activity enrichment
201 can be found in Supplementary Table 3.
202

203 **Chromatin accessibility and gene expression jointly define fate predictive cell state**
204 Our above state-fate analysis suggests that lineage-specific changes in gene expression are
205 accompanied by extensive epigenetic remodeling, rendering the genome more accessible to fate-
206 specifying TFs. Previous analysis has suggested that cell states hidden from transcriptional
207 profiling play a role in fully defining fate-associated changes in cell state[13]. Changes in chromatin
208 accessibility could account for some of this hidden variance and we tested this hypothesis by
209 assessing whether cell fate can be accurately predicted from early state using our multiomic clonal
210 data.
211 We trained machine learning models to predict clonal cell fate from gene expression or
212 chromatin accessibility profiles of Day 2.5 sisters (**Ext Fig. 5a**). We tested three different
213 architectures: Logistic Regression, Random Forest, and LightGBM, and assessed model
214 performance using prediction accuracy (**Ext Fig 5b**). Overall, Random Forest models performed
215 the best and were used for all downstream analysis. For gene expression, we trained a
216 classification model to predict clonal fate using expression of the three thousand most highly
217 variable genes (HVG) and obtained an accuracy of 75.6% (**Fig. 2j, Ext Fig. 5c**). For chromatin
218 accessibility, we used Day 2.5 imputed TF activity scores (**Methods**) for 884 TF motifs to predict
219 clonal fate and obtained an accuracy of 72.7% (**Fig. 2j**). Notably, an RNA model trained on
220 expression levels of TFs, obtained from the Catalog of Inferred Sequence Binding Preferences
221 (CIS-BP) database, only scored only 63.8% on prediction accuracy (**Fig. 2j**). The significantly
222 lower predictive performance of TF expression compared to TF activity could be attributed to
223 either technical dropout in scRNA-seq or significantly higher lineage specific priming of TF binding
224 sites compared to TF expression, or a combination of both.
225 To assess fate-specific priming in different functional regions of the epigenome, we
226 computed TF activity scores using subsets of accessible peaks and compared fate prediction
227 performance across these feature spaces. Specifically, we computed TF activity scores using
228 only promoter, distal, exonic, or intronic peaks and trained fate prediction models with each. We
229 observed significant variation in performance between different ATAC models, indicating different
230 levels of fate-specific epigenetic priming across functional regions of the genome (**Ext Fig. 5d**).
231 This variation was independent of the number of peaks used to compute each set of TF activity
232 scores (**Ext Fig. 5d**). Distal and Intronic were the best performing models, comparable in
233 performance to the full peak set model ('All'). Promoter and Exonic models performed significantly
234 worse, suggesting that fate-specifying epigenetic changes during these early stages were
235 dominated by changes in distal regulatory regions of the epigenome rather than accessibility of
236 genes themselves. This observation is reinforced by the persistence of TF enrichment trends

237 across state groups in distal and intronic subsets but not in the exonic and promoter subsets (**Ext**
238 **Fig. 5e**). We confirmed these results using SHAP, a game theoretic approach to quantify the
239 contributions of individual input features in explaining the output of a machine learning model[29].
240 Indeed, SHAP analysis showed that in the better-performing models, an increase in CEBP/A motif
241 accessibility and an increase in MECOM motif accessibility were better predictors of Monocyte
242 and Ery/Meg fates, respectively, suggesting a lack of functional priming in the promoter-proximal
243 accessible genome (**Ext Fig. 5f, g**).
244 Finally, we tested whether combining RNA and ATAC features is more predictive of fate
245 than either individual modality. For this, we trained a combined RNA and ATAC model where RNA
246 and ATAC Day 2.5 sister cells within the same clone were paired randomly, and their combined
247 gene expression and TF activity signatures were used to predict clonal fate label. This analysis
248 was limited to multiomic state-fate clones. The combination of both state modalities was
249 significantly better at predicting fate (mean accuracy score = 86.5%) compared to either individual
250 modality or pairs of unrelated RNA and ATAC state cells (**Fig. 2j**). These results show that both
251 gene expression and chromatin accessibility jointly comprise cell states that define future cell fate.
252 Moreover, these modalities consist of non-redundant and highly complementary state information,
253 as a combination of both predicts cell fate much more accurately than each modality in isolation.
254
255 **Dissecting clonal dynamics of direct reprogramming**
256 Our application of CellTag-multi to hematopoiesis demonstrated the method's utility to capture
257 informative gene regulatory dynamics in a well-characterized differentiation paradigm. We next
258 applied CellTag-multi to a less defined system — the direct reprogramming of MEFs to iEPs driven
259 by retroviral overexpression of Hnf4α and Foxa1[7,30,31]. Direct lineage reprogramming presents a
260 unique paradigm of cell identity conversion, with cells often transitioning through progenitor-like
261 states or acquiring off-target identities[32,33]. Such non-linear fate dynamics can be challenging to
262 assess, especially when relying solely on the computational inference of cell fate trajectories[12].
263 Ground truth lineage tracing serves as a crucial resource for dissecting lineage-specific cell state
264 changes during direct reprogramming[7]. Originally reported to yield hepatocyte-like cells[30], we
265 have previously shown that Hnf4α and Foxa1 overexpression in MEFs generates cells with the
266 broader potential to functionally engraft liver and intestine[16,31,34]. This prompted their re-
267 designation as 'induced Endoderm Progenitors' (iEPs). More recently, we have further
268 characterized the similarity of long-term cultured iEPs to regenerating Biliary Epithelial Cells
269 (BECs)[35].

Using our original CellTag-based lineage tracing, we identified two distinct iEP reprogramming trajectories: a successful 'reprogrammed' trajectory, characterized by endodermal and hepatic gene expression, and a 'dead-end' trajectory, defined by a failure to extinguish the starting fibroblast identity[7]. Further work demonstrated key functional differences between these fates, with successfully reprogrammed cells harboring the potential to engraft acutely damaged mouse intestine[16]. Our previous lineage tracing suggests that the reprogrammed and dead-end fates are determined in the early stages of fate conversion[7]. However, our original CellTagging methodology did not capture any epigenetic information and only sparsely sampled early state clones, limiting mechanistic insight into these initial reprogramming stages.

Here, we deployed CellTag-multi in iEP reprogramming, modifying our clonal resampling strategy to optimize state-fate analysis (**Fig. 3a**). First, we transduced MEFs with Hnf4α and Foxa1 for 48 hours to initiate reprogramming, in two independent biological replicates. During the last 12 hours of this 48-hour period, we transduced cells with the complex CellTag-multi library, enabling clonal relationships to be tracked. 72 hours following the final viral transduction (Reprogramming Day 3), we collected two-thirds of the cells for single-cell RNA and ATAC profiling (state sample) and re-plated the remaining cells. Subsequent samples were collected on Days 12 and 21 (fate samples) to assess reprogramming outcome. We also profiled the starting MEF population (scATAC-seq, this study; scRNA-seq from a previous study[7])), resulting in a total of 466,459 single-cells (scATAC-seq: 223,686; scRNA-seq: 242,863) in the final dataset after quality filtering (**Ext Fig. 6a, b**). We identified a total of 8,502 clones, containing 46,438 cells (Replicate 1: 3,068 clones; Replicate 2: 5,416 clones, average clone sizes of 4.8 and 5.9 cells/clone, respectively (**Ext Fig. 6c, d**)). We identified 1,428 'state-fate' clones across both replicates, defined as clones that spanned state (Day 3) and at least one fate time point, Day 12 or Day 21 (**Ext Fig. 6d**).

Following dimensionality reduction and clustering of the co-embedded RNA and ATAC datasets, clone-cell embedding was performed (**Fig. 3b, Ext Fig. 6e, f, g**). We annotated Day 12 and 21 fate clusters ('reprogrammed,' 'dead-end,' and 'transition') based on expression and accessibility of known reprogramming associated genes, and unsupervised cell-type classification based on transcriptional state using Capybara[35] (**Fig. 3c; Ext Fig. 7a, b**). In line with our previous reports[7,16,35,36], reprogrammed cells express epithelial and iEP markers, *Cdh1* and *Apoa1*, respectively. Dead-end cells are characterized by the retention of fibroblast gene expression but are still transcriptionally distinct from MEFs, expressing low levels of iEP markers and several dead-end-specific genes such as *Sfrp1,* a Wnt signaling modulator[7] (**Ext Fig. 7b, c**). Transition

304 cells represent states in between MEFs and reprogrammed/dead-end identities. Following cluster
305 annotation, we assigned fate labels to each state-fate clone. As the majority of state-fate clones
306 showed high fate-bias, we assigned clonal fate based on the most abundant cell annotation
307 amongst the fate sisters (**Fig. 3d**), identifying 1,009 reprogrammed, 2,493 dead-end and 1,371
308 transition clones. Dead-end and reprogrammed clones displayed a lineage-specific increase in
309 accessibility of known marker genes (**Fig. 3e**).
310 Using clonal information, we linked each reprogrammed and dead-end clone to its Day 3
311 state sisters, allowing us to track changes in cell identity longitudinally (**Fig. 3f**). Comparing
312 Capybara transcriptional cell identity scores across lineages, we found that iEP identity scores
313 were consistently higher along the reprogrammed lineage compared to the dead-end lineage.
314 MEF identity scores, while significantly higher along the dead-end lineage, exhibited a steep
315 decline after Day 12 coinciding with an increase in dead-end transcriptional identity score (**Fig.
316 3g, Ext Fig. 7d**). This suggested a delayed departure from MEF identity to an alternate cell state.
317 We observed high levels of clonal expansion along both lineages (**Fig. 3h, i**). These observations
318 suggest that despite retaining expression of canonical fibroblast marker genes, dead-end cells
319 are a fundamentally distinct, off-target cell state and reprogramming outcome. Thus, the
320 'reprogrammed' and 'dead-end' fates are better described as 'on-target' and 'off-target'
321 reprogramming, respectively.
322
323 **Linking early state to fate reveals molecular features of off-target reprogramming**
324 Next, to identify early state changes that regulate entry onto distinct fate trajectories, we focused
325 on Day 3 state clones destined to on-target (reprogrammed) or off-target (dead-end)
326 reprogramming fates. From assessing the distribution of Day 3 sisters destined to either of the
327 two fates, it is evident that they are not localized to defined clusters (**Ext Fig. 8a, b**). Further,
328 trajectory inference using CellRank[37] fails to reveal these initial states (**Ext Fig. 8c**),
329 demonstrating the importance of ground truth lineage tracing. We found that both Day 3 gene
330 expression and TF activities were highly predictive of clonal fate. Similar to our analysis of
331 hematopoiesis, fate prediction accuracy was significantly higher when both modalities were
332 considered, as compared to either modality individually. Further, distal and intronic peaks were
333 more predictive of fate than proximal and exonic (**Ext Fig. 8d, e**).
334 To identify early molecular signatures of lineage specification, we compared gene
335 expression, chromatin accessibility, and TF activity scores across MEFs and Day 3 state sisters
336 grouped by fate outcome. Comparing gene expression enrichment across the three groups, 2,116
337 genes were differentially enriched with 1,582 enriched genes uniquely defining each group (**Fig.**

338 **4a, Ext Fig. 8f**). While some genes displayed transient fate-specific expression, others
339 consistently increased over time in a lineage-specific manner (**Supplementary Table 4**). Early
340 iEP marker genes such as *Apoa1* were enriched in both on- and off-target trajectories on Day 3,
341 consistent with our previous observation that most cells initiate reprogramming[7] (**Ext Fig. 8f, g**).
342 On-target (reprogrammed) enriched genes included *Krt19*, a marker of BECs, Wnt signaling
343 associated genes *Wnt4*, *Anxa8,* and epithelial marker *Ezr* (**Fig. 4b, Supplementary Table 5**).
344 Top off-target (dead-end) related genes included canonical smooth muscle markers *Acta2* and
345 *Tagln* and other mesenchymal genes such as *Ptn,* and *Ncam1*, suggesting broad engagement of
346 mesenchymal programs, in addition to *Sfrp1*, a Wnt signaling pathway inhibitor (**Fig. 4b,**
347 **Supplementary Table 5**).
348 Comparing genome-wide chromatin accessibility revealed 21,720 Differentially Enriched
349 Regions (DERs) across Day 3 on-target and off-target destined cells and uninduced MEFs,
350 indicating extensive fate-specific epigenetic reconfiguration during early reprogramming (**Fig. 4c,**
351 **Supplementary Table 6**). DERs were enriched for distal and intergenic peaks, suggesting
352 epigenetic re-patterning of distal regions as a driver of cell fate conversion, consistent with our
353 above observations in hematopoiesis (**Ext Fig. 8h**). Motif analysis revealed enrichment of
354 reprogramming and hepatic TFs in on-target DERs, and several TFs with documented roles in
355 mesenchymal fates[38,39] in off-target DERs (**Ext Fig. 8i, j**). Using our paired RNA and ATAC data,
356 we linked accessible peaks to genes and identified 37,058 putative cis-regulatory elements
357 (CREs)[40] (**Fig 4c**, **Supplementary Table 6, Methods**). Gene-linked peaks were enriched for
358 enhancer-like signatures (ELS) from the ENCODE candidate CRE database[41] (**Methods**, **Ext Fig.**
359 **8k**). Genes linked to on-target and off-target DERs displayed fate-specific expression patterns
360 (**Fig. 4d, Ext Fig. 8l**). On-target DERs consisted of several CREs linked to endodermal genes,
361 such as *Alb*, *Foxq1,* and *Creb3l2.* In contrast, off-target DERs contained CREs linked to
362 mesenchymal genes such as *Ncam1*, a modulator of Mesenchymal Stromal Cell migration[42],
363 *Fbln2*, a mesenchymal gene associated with embryonic heart development[43], and *Vegfd*, a
364 regulator of angiogenesis[44] and endothelial differentiation of bone marrow-derived mesenchymal
365 stem cells[45] (**Fig. 4c**). In several instances, this analysis captured lineage-specific changes in
366 accessibility of CREs before significant changes in gene expression were detected. For instance,
367 a *Vegfd*-linked CRE overlapping with an ENCODE enhancer displayed enrichment in dead-end
368 destined cells (Day 3), while expression changes were not detectable until Day 12. Similar
369 regulatory changes were observed for *Aox3*[46], a liver-associated aldehyde oxidase, and *Col28a1,*
370 an oligodendrocyte enriched collagen[47], prior to changes in gene expression (**Fig. 4e,**
371 **Supplementary Table 6**).

372 To identify functional changes in chromatin accessibility on a genomic scale, we compared
373 inferred TF activities across on-target and off-target destined cells and uninduced MEFs. To
374 preclude potential false positives, we discarded all TFs with low correlation (< 0.3) with their
375 respective gene activity scores, identifying 47 uniquely enriched TFs (**Fig. 4f, Ext Fig. 8m,**
376 **Supplementary Table 7**). On-target destined cells were highly enriched for the two
377 reprogramming TFs, FOXA1, and HNF4A. Other on-target associated TFs included FOXD2,
378 FOXO1, and NR1H3, a hepatic fate-specifying TF[48] (**Fig. 4f**). We identified a set of nine TFs
379 uniquely enriched in off-target destined cells (**Fig. 4f (black bar), g**). Several of these TFs
380 (Zfp281, Cebpb, Gata6, Hivep3) have been previously documented to play a role in regulating
381 mesenchymal cell identities[49–52]. Surveying the expression data, none of the off-target TFs display
382 a similar fate-biased enrichment (**Fig. 4g, Ext Fig. 8n**), highlighting the importance of lineage-
383 specific chromatin profiling in identifying these targets. This lack of enrichment could be due to
384 technical dropout during scRNA-seq or due to secondary mechanisms regulating the genomic
385 engagement of these TFs.
386 Altogether, our lineage-specific multiomic assessment of iEP generation demonstrates
387 clear early molecular differences associated with reprogramming outcomes. Indeed, from as early
388 as reprogramming day 3, cells on the dead-end lineage exhibit unique characteristics. Rather
389 than retaining MEF identity, we observe that the dead-end lineage constitutes a highly
390 proliferative, mesenchymal cell state with unique markers and regulatory changes, thus
391 representing an 'off-target' reprogrammed state. The early specification of this state is supported
392 by our GRN inference using CellOracle[36], suggesting that network reconfiguration is unique to
393 each trajectory and is established early in the reprogramming process. CellTag-multi has the
394 potential to define the molecular features of these early states, offering deeper mechanistic insight
395 into the reprogramming process.
396
397 **Foxd2 and Zfp281 as drivers of on- and off-target reprogramming**
398 Higher accessibility of both motifs and genomic targets[53] of FOXA1 and HNF4A in on-target cells
399 on Day 3 suggests significant differences in genomic engagement of the reprogramming TFs
400 between the two fate outcomes (**Fig. 5a, Ext Fig. 9a**). This could, at least in part, be explained
401 by differential expression levels of the *Hnf4α-Foxa1* transgene across the two lineages, with off-
402 target destined cells displaying significantly lower transgene expression (**Fig. 5a**; Mann Whitney
403 Wilcoxon test; p-value = 6.5e-42). However, we have also previously described an off-target
404 trajectory expressing high transgene levels, suggesting additional mechanisms influencing
405 genomic engagement by the reprogramming TFs[36].

406 Outside of FOXA1, and HNF4A, we identified FOXD2 as the top on-target fate-specifying
407 TF candidate (**Fig. 5b, Ext Fig. 9b**). Adding Foxd2 to the Foxa1 and Hnf4α reprogramming
408 cocktail led to significantly increased expression of the iEP marker *Cdh1* and decreased
409 expression of mesenchymal marker *Tagln* on reprogramming day 12 (t-test; p-values: *Cdh1* =
410 0.03; *Tagln* = 0.006; 2 biological replicates; 2 technical replicates **Ext Fig. 9c**). In addition, colony
411 formation assays showed a significant increase in the number of CDH1-positive colonies formed
412 with the addition of Foxd2 to the standard iEP reprogramming cocktail (t-test; p-value=0.045; 2
413 biological replicates; **Fig. 5c**), validating its role in improving on-target fate conversion.
414 The top off-target-enriched candidate was ZFP281, a Zinc Finger protein (**Fig. 5d, Ext**
415 **Fig. 9d**). Zfp281 is a known regulator of cell fate in mouse embryonic stem cells[54] and promotes
416 epithelial-to-mesenchymal transitions[55]. To further confirm the inferred enrichment of ZFP281 TF
417 activity in off-target fated cells, we performed Tomtom motif similarity analysis[56] to identify TFs
418 that share a motif similar to ZFP281. We found four other TF motifs that were both significantly
419 similar to the ZFP281 motif (adjusted p-value < 0.05) and were enriched in off-target destined
420 cells. Amongst these TFs, ZFP281 displayed the highest enrichment in the off-target lineage both
421 in terms of gene expression and TF activity (**Ext Fig. 9e**). Additionally, single-cell accessibility of
422 ZFP281 genomic targets[54] was positively correlated with inferred ZFP281 TF activity (Pearson's
423 correlation coefficient = 0.53; **Ext Fig. 9f**) and ZFP281 regulated genes[57] were significantly more
424 predictive of cell fate as compared to a size-matched set of random genes (Mann Whitney
425 Wilcoxon test; p-value = 2.248e-09; **Ext Fig. 9g**), further confirming its role in off-target fate
426 specification during iEP reprogramming. Notably, both *Zfp281* and *Foxd2* failed to show a strong
427 lineage-specific bias in gene expression levels, highlighting the unique insights offered by
428 multiomic lineage tracing in the identification of fate-specifying TFs (**Ext Fig. 9h**).
429 Indeed, inclusion of Zfp281 along with Foxa1 and Hnf4α in the reprogramming cocktail
430 resulted in a moderate but statistically significant reduction in the number of CDH1-positive
431 colonies (t-test; p-value = 0.017; **Fig. 5e**). To further characterize the role of Zfp281 in
432 reprogramming, we performed both overexpression (OE) and shRNA mediated knockdown (KD)
433 of Zfp281, along with respective control samples, and profiled cells with single-cell sequencing on
434 reprogramming day 14 (**Fig. 5f, g, Ext Fig. 10a**). We found that the rate of reprogramming (both
435 on- and off-target) increased with increasing *Zfp281* expression (**Ext Fig 10b**), suggesting a role
436 for Zfp281 in accelerating fate conversion in iEP reprogramming. Moreover, we identified a distinct
437 subpopulation of cells, predominantly consisting of Zfp281 KD cells that were depleted for
438 expression of key markers of both on-target and off-target reprogramming such as *Apoa1* and
439 *Ctla2a* (**Ext Fig 10c-e**). These cells were enriched for MEF and early off-target marker gene

expression, depleted for both off-target and on-target markers genes from Day 21 (obtained from our lineage analysis; **Ext Fig. 10f-h**) and thus likely represent a "stalled" cell state due to reduced *Zfp281* expression levels. Despite its acceleration of cell fate conversion broadly, we found that Zfp281 shifted the identity of reprogrammed cells away from an iEP-like state and towards a dead-end/off-target-like state consistently across the OE and KD experiments (**Fig. 5h, i**), confirming a role for Zfp281 in biasing cells towards an off-target fate, as suggested by our lineage tracing analysis. This finding also explains the reduced number of CDH1-positive colonies observed in our colony formation assay, despite the increase in total number of on-target reprogrammed cells upon Zfp281 overexpression.

Finally, a key downstream effector of Zfp281 is TGF-β signaling[49,58], an Epithelial-to-Mesenchymal Transition (EMT) associated pathway[59]. Indeed, TGF-β pathway activity, as inferred using PROGENy[60] (**Methods**), increased with *Zfp281* OE and decreased with *Zfp281* KD, suggesting active regulation of TGF-β signaling by Zfp281. Given that on-target reprogramming is characterized by cellular epithelialization and off-target reprogramming is characterized by activation of broad mesenchymal programs, we hypothesized that increased TGF-β signaling mediated via Zfp281 acts as a barrier to on-target reprogramming. Indeed, inhibition of TGF-β signaling during iEP reprogramming using the small molecule SB431542[61] led to a significant increase in expression of reprogramming marker genes *Apoa1* and *Gsta4* and a significant decrease in mesenchymal/off-target genes such as *Serpine1, Snail1, Col1a2* (**Fig. 5k**). This was accompanied by an increase in epithelial/iEP-like morphology as early as day 3 of reprogramming (**Ext Fig 10i**) suggesting a crucial role for TGF-β signaling, downstream of Zfp281, in determining fate outcome during iEP reprogramming.

Discussion

Here we have presented CellTag-multi, a method for multiomic single-cell lineage tracing. In the context of hematopoiesis, we have used CellTag-multi to map transcriptional and epigenomic states of progenitor cells and link them to clonal fate, recapitulating enrichment of known lineage-specific cell state signatures across progenitor populations. With chromatin state, we showed that lineage-specific epigenetic priming is associated with changes in accessibility of known fate-specifying TF motifs and that such changes occur primarily in the regions of the genome distal to promoters. Previous analysis has demonstrated the inability of early transcriptional state alone in predicting cell fate and posited a role for alternate cell state modalities[13]. By exploiting multiomic clonal relationships, we demonstrated that the predictability of cell fate from state is significantly improved when both early transcriptional and epigenomic state are considered, as opposed to

474 either modality individually, suggesting that the RNA and ATAC modalities consist of non-
475 redundant and highly complementary state information.

476 Our application of CellTag-multi to the less characterized paradigm of iEP reprogramming
477 generated similar observations, where multiomic clonal data captured in the early stages of fate
478 conversion is highly predictive of reprogramming outcome. Again, fate-specifying epigenetic
479 changes during early stages of differentiation are dominated by changes in distal regulatory
480 regions of the epigenome. Further, we have been able to molecularly characterize the 'dead-end'
481 state as a highly proliferative, mesenchymal-like cell state, representing an 'off-target'
482 reprogrammed state. Indeed, a similar state has been reported in direct reprogramming of
483 mesenchymal stromal cells to induced hepatocytes, revealing the appearance of *Acta2*-
484 expressing mesenchymal cells during the reprogramming process[62]. Outside of the hepatic
485 lineage, off-target identities have been reported in other reprogramming paradigms[33,63],
486 suggesting that this may be a more general feature of lineage reprogramming.

487 Our multiomic lineage tracing demonstrates the establishment of on- and off-target
488 trajectories from early stages, supported by our earlier transcriptome-based lineage tracing of iEP
489 reprogramming[7] and GRN inference[36]. However, given the single modality capture of relatively
490 few clones in that earlier study, we were not able to comprehensively characterize early molecular
491 states. Here, the collection of ground truth data on lineage, transcriptome, and epigenome has
492 allowed us to better characterize these distinctive early states, enabling novel mechanistic
493 insights into reprogramming. We have shown crucial early differences in gene regulation that lead
494 to distinct reprogramming outcomes. Specifically, we have identified and experimentally validated
495 that Foxd2 promotes successful reprogramming, while Zfp281 activity leads to engagement with
496 an off-target trajectory. Differences in reprogramming TF levels may account for these early
497 differences. However, lower levels of exogenous TF expression do not simply lead to
498 reprogramming failure, as the off-target fate is molecularly unique from fibroblasts and could be
499 considered a reprogramming byproduct in itself. These results suggest that the stoichiometry of
500 TF overexpression in these reprogramming models may offer further insight into how TFs control
501 cell identity. Single-cell analysis of TF binding could provide further insights into the role of
502 differential binding of the two reprogramming TFs in specifying off-target fate.

503 Our recovery of Foxd2 and Zfp281 as novel regulators of early-stage reprogramming was
504 not possible from differential gene expression analysis alone, demonstrating the utility of CellTag-
505 multi. Our data suggests off-target enriched Zfp281 activity from early stages of reprogramming.
506 From our experimental validation, we found that knockdown of Zfp281 expands a population of
507 cells in a 'stalled' state, where they fail to extinguish fibroblast gene expression while upregulating

508 off-target cells. Conversely, overexpression of Zfp281 helps accelerate fate conversion, resulting
509 in a considerable increase in reprogramming efficiency. However, Zfp281 still draws the
510 reprogrammed cells toward an off-target, mesenchymal-like state. A role for this TF in driving
511 broad mesenchymal expression programs, including components of the TGF-β signaling
512 pathway, has recently been described[49]. Here, we demonstrate that the inhibition of TGF-β
513 signaling enhances on-target marker expression while decreasing off-target gene expression.
514 These results suggest a potential strategy to enhance on-target reprogramming, where Zfp281
515 expression can help erase the starting cell identity while blocking downstream TGF-β signaling
516 might prohibit entry onto the off-target trajectory.

517 Altogether, the data we present here across two distinct biological systems demonstrates
518 that lineage-specific capture of gene expression and chromatin accessibility provides rich
519 information on gene regulation, offering unique mechanistic insights into the specification and
520 maintenance of cell identity. More widely, single-cell lineage tracing has revealed distinct, clonally
521 heritable transcriptional states across various biological systems[64–66]. These phenotypic
522 differences, arising from seemingly non-genetic sources, have strong biological implications. For
523 example, clonal variability in cell state has been shown to impact malignant clonal expansion and
524 efficacy of drug treatment in cancer cells[64,66]. Given its versatility and ease of use, we envision
525 that CellTag-multi can be readily applied to such biological questions and help reveal the
526 mechanistic basis of clonally heritable cell states.

527 Finally, we have developed CellTag-multi to work independently with scRNA-seq and
528 scATAC-seq, as existing single-cell methods that co-assay multiple modalities from the same
529 cell[67–70] can suffer from lower data quality compared to methods that profile each modality
530 individually. Further, enabling the capture of lineage in parallel with chromatin accessibility
531 provides users with additional flexibility for experimental design. Advances in single-cell
532 technologies are allowing measurement of an ever-increasing number of cellular modalities[71,72].
533 A similar expansion in lineage tracing assays will complement these new methods with multiomic,
534 clonal tracking of cell state and enable deeper mechanistic insight into the regulation of cell
535 identity and clonal heritability of cell state. CellTag-multi, with its cell lineage read out alongside
536 gene expression and chromatin accessibility, paves the way for such multiomic, single-cell lineage
537 tracing methods.

538

539 **Acknowledgments**

540 We thank members of the Morris laboratory for helpful discussions. This work was funded by the
541 National Institute of General Medical Sciences R01 GM126112, and Silicon Valley Community

Foundation, Chan Zuckerberg Initiative Grant DAF2021-238797, both to S.A.M. S.A.M. is supported by an Allen Distinguished Investigator Award (through the Paul G. Allen Frontiers Group), a Vallee Scholar Award, a Sloan Research Fellowship, and a New York Stem Cell Foundation Robertson Investigator Award; K.K. is supported by a Japan Society for the Promotion of Science Postdoctoral Fellowship; N.Y. is supported by McDonnell International Scholars Academy fellowship.

Author Contributions

Conceptualization, Methodology, K.J., S.A.M.; Software, K.J.; Formal Analysis, K.J., N.Y.; Experimentation, K.J., M.T.A., H.W., X.Y., S.A.M., K.K., G.R.G.; Data Curation, K.J., M.T.A.; Writing – Original Draft, K.J., S.A.M.; Writing – Review & Editing, K.J., M.T.A., H.W., N.Y., K.K., G.R.G., S.A.M.; Visualization, K.J., S.A.M.; Funding Acquisition, Resources, Supervision, S.A.M.

Declaration of Interests

S.A.M. and G.R.G. are cofounders of CapyBio LLC.

Figure 1

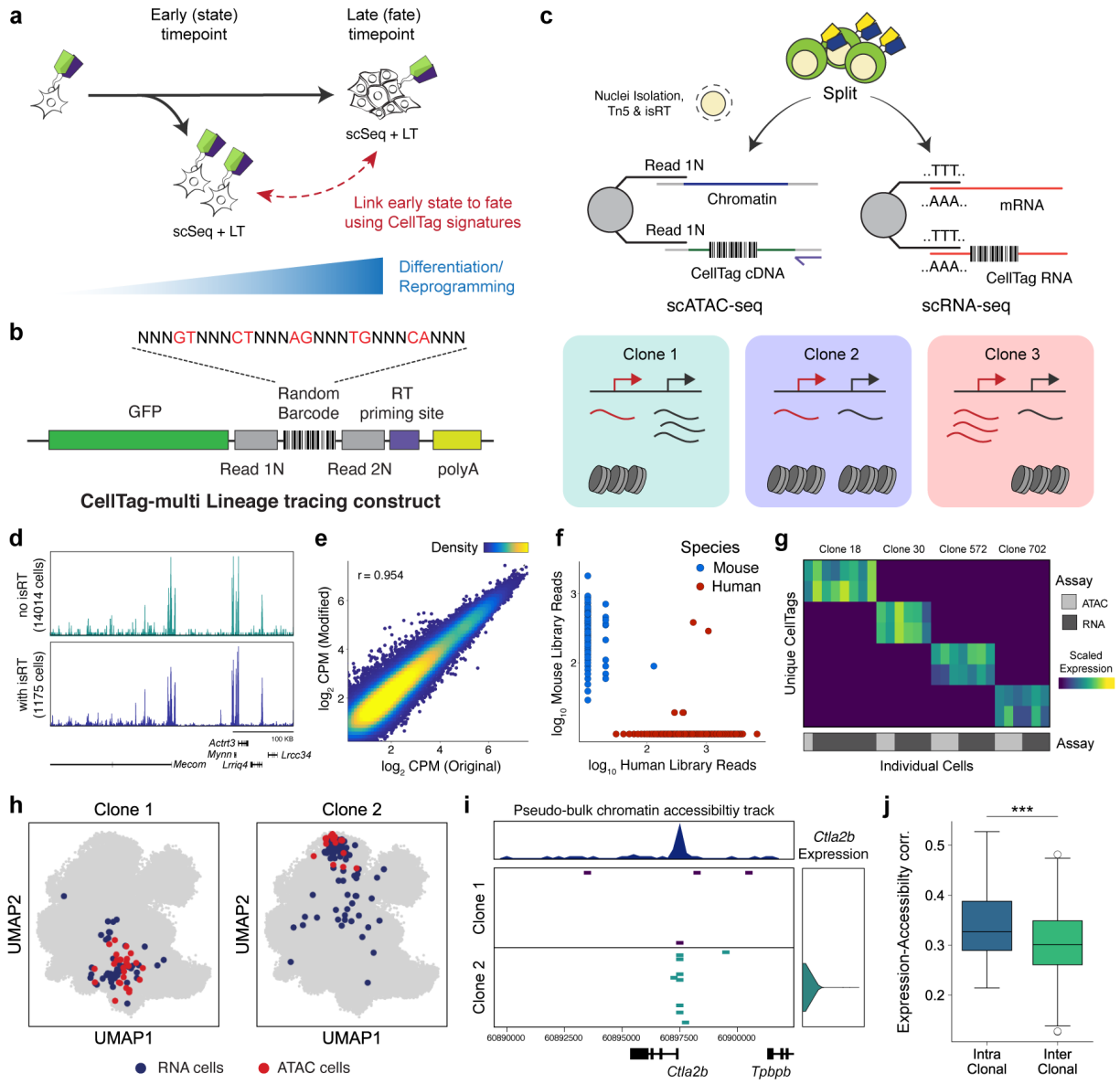

Figure 1. CellTag-multi allows simultaneous capture of lineage information with gene expression and chromatin accessibility. (**a**) A framework for relating early cell state with fate using single-cell lineage tracing. (**b**) Schematic depicting the CellTag-multi lineage tracing construct. (**c**) Schematic detailing parallel capture of CellTags during scRNA-seq and modified scATAC-seq library preparation, using targeted isRT of CellTags in intact nuclei. CellTag-multi enables simultaneous clonal tracking of transcriptional and epigenomic state. (**d**) Browser tracks comparing chromatin accessibility signal across aggregated scATAC-seq profiles generated using the original and modified library preparation methods. (**e**) Scatterplot comparing log

566 normalized reads in ATAC peaks across aggregated scATAC-seq profiles generated with the
567 original and modified library preparation methods. (r = Pearson Correlation Coefficient). (**f**) Plot
568 for the human-mouse species mixing experiment depicting the number of CellTag reads/cell from
569 each CellTag library. (**g**) Heatmap showing scaled CellTag expression in scRNA-seq and
570 scATAC-seq sisters for four multiomic clones identified in a population of expanded
571 reprogramming fibroblasts. (**h**) Joint UMAP of RNA and ATAC cells with two clones (clone 1 and
572 clones 2) cells projected, along with assay information. (**i**) Browser track showing single-cell
573 accessibility at the *Ctla2b* locus and *Ctla2b* gene expression across clones 1 and 2. Top Panel:
574 Pseudo-bulk accessibility signal at the *Ctla2b* locus. (**j**) Box plots comparing intra- and inter-clonal
575 correlation between clonally aggregated gene expression and gene activity scores in the
576 reprogramming dataset (n = 62 clones used; Mann Whitney Wilcoxon test; p-value = 5.39e-4).

Figure 2

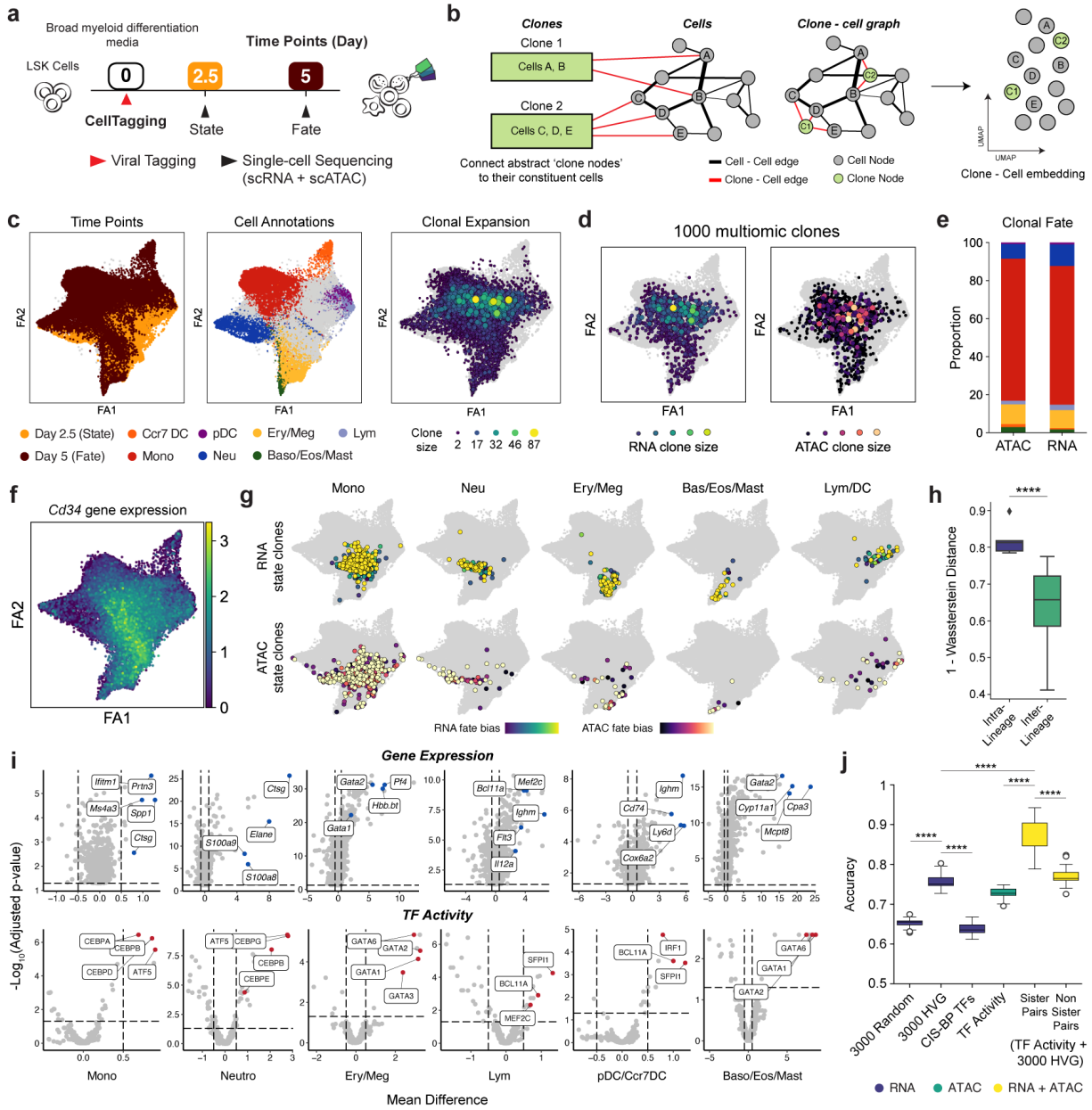

577

578 **Figure 2. Application of CellTag-multi to link early hematopoietic cell state with fate.** (**a**)
579 Schematic detailing the experimental design for the *in vitro* hematopoiesis state-fate experiment.
580 (**b**) Workflow for joint embedding of cells and clone nodes. (**c**) Clone-cell embedding UMAPs with
581 time point and cell fate information projected onto cells (right and center panels) and clonal
582 expansion information projected onto clones (left panel). Only major cell fates are highlighted,
583 detailed annotations are shown in **Ext Fig. 3j** (Mono: Monocytes; Neu: Neutrophils; Lym:
584 Lymphoids; Ery: Erythroids; Meg: Megakaryocytes; Baso: Basophils; Eos: Eosinophils; Mast:

585 Mast Cells; pDC: plastoid Dendritic Cells). (**d**) UMAPs with RNA and ATAC clonal expansion
586 information projected onto a thousand random multiomic clones. Both modalities display biased
587 expansion of early myeloid cells, consistent with our differentiation culture conditions. (**e**) Bar plot
588 depicting distribution of cell fates across RNA and ATAC clones (Fates are colored as in **Fig. 2c**).
589 (**f**) UMAP with scaled *Cd34* expression level, a marker of Hematopoietic Stem and Progenitor
590 Cells (HSPCs), projected onto the scRNA cells. (**g**) UMAPs with state (Day 2.5) sub-clones for
591 each major lineage highlighted along the differentiation continuum for both single-cell modalities,
592 with fate bias information projected. (**h**) Box plot comparing overlap between RNA and ATAC
593 state sub-clones within and across cell fates (Mann Whitney Wilcoxon test; p-value = 3.76e-5). (**i**)
594 Volcano plots summarizing the results of differential feature enrichment analysis for each group
595 of state sub-clones across for scRNA (top panel) and scATAC modalities (bottom panel). (**j**) Box
596 plot summarizing accuracy scores of trained state-fate prediction models. Machine learning
597 partially predicts cell fate from Day 2.5 state across both modalities. However, predictive
598 performance increases significantly when both are considered together, highlighting the existence
599 of unique functional priming in both gene expression and chromatin accessibility state (Mann
600 Whitney Wilcoxon test; p-values: **** = $p < 0.0001$, HVG: Highly Variable Genes, n = 25 accuracy
601 values for each model (**Methods**)).

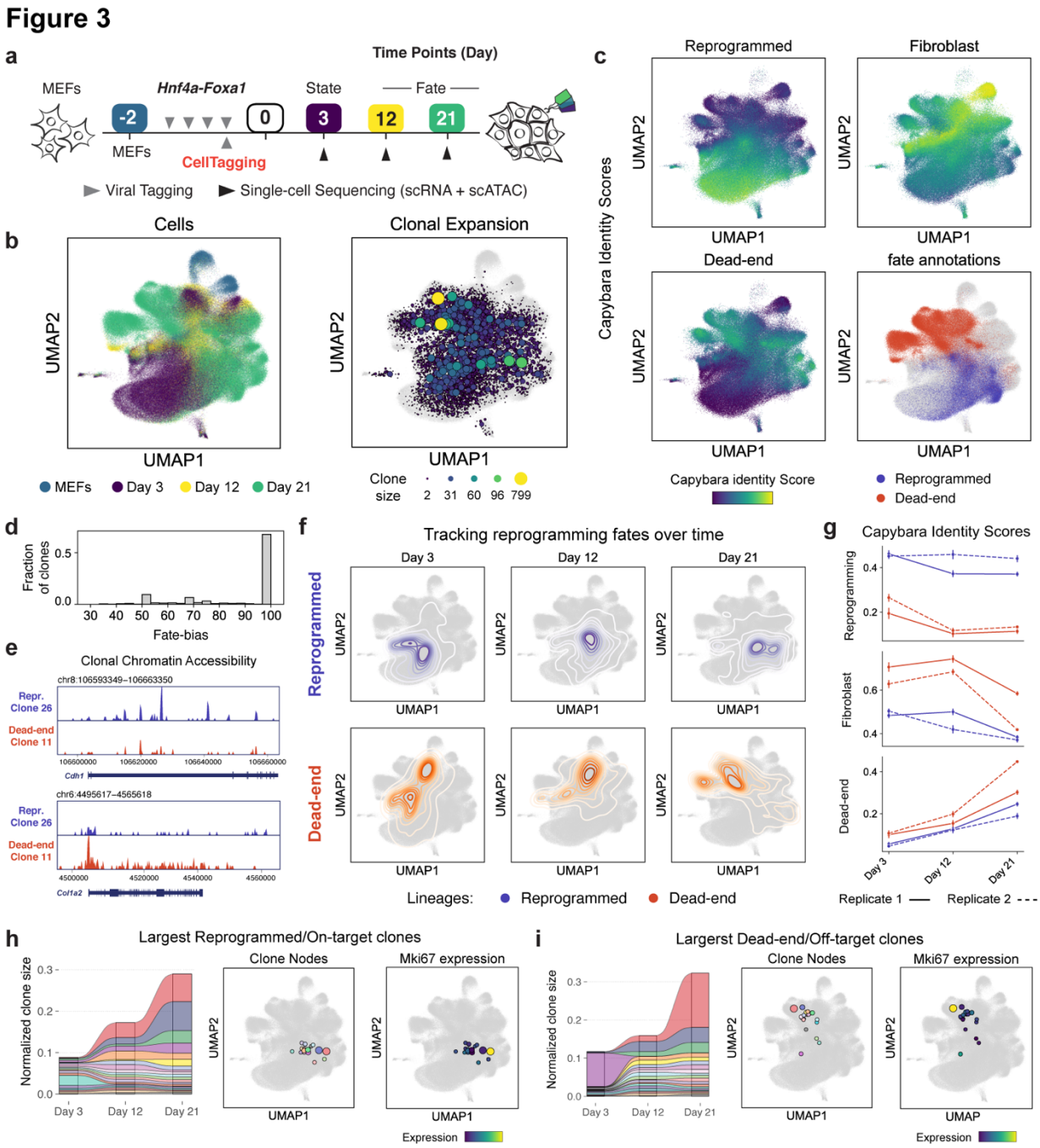

Figure 3. Application of CellTag-multi to dissect clonal fate dynamics in direct reprogramming. (**a**) Experimental design for the direct reprogramming state-fate experiment. (**b**) Cells from both scRNA-seq and scATAC-seq, across all time points, were co-embedded with clones and visualized using a UMAP. (Left Panel) Time point information projected on cells. (Right Panel) Clonal expansion visualized using clone nodes. (**c**) Capybara transcriptional identity scores projected on scRNA-seq cells for reprogrammed, dead-end and fibroblast cell identities,

609 based on a previous lineage tracing dataset[7]. Cell fates were annotated for Days 12 and 21.
610 Reprogrammed and dead-end cell fates are highlighted (Lower Right Panel). (**d**) Histogram of
611 fate bias across all state-fate clones. (**e**) Clonal chromatin accessibility browser tracks for two
612 dead-end and reprogramming clones. (**f**) Contour plots showing longitudinal tracking of cell fates
613 enabled by CellTagging. (**g**) Transcriptional identity dynamics tracked along both lineages. Dead-
614 end cells depart from a MEF like identity and acquire an off-target reprogrammed state. Significant
615 clonal expansion is observed along both lineages, as depicted via alluvial plots, clone nodes and
616 clonal expression levels of *Mki67* (a proliferation marker gene) in the 20 largest (**h**)
617 reprogramming/on-target and (**i**) dead-end/off-target clones.

Figure 4

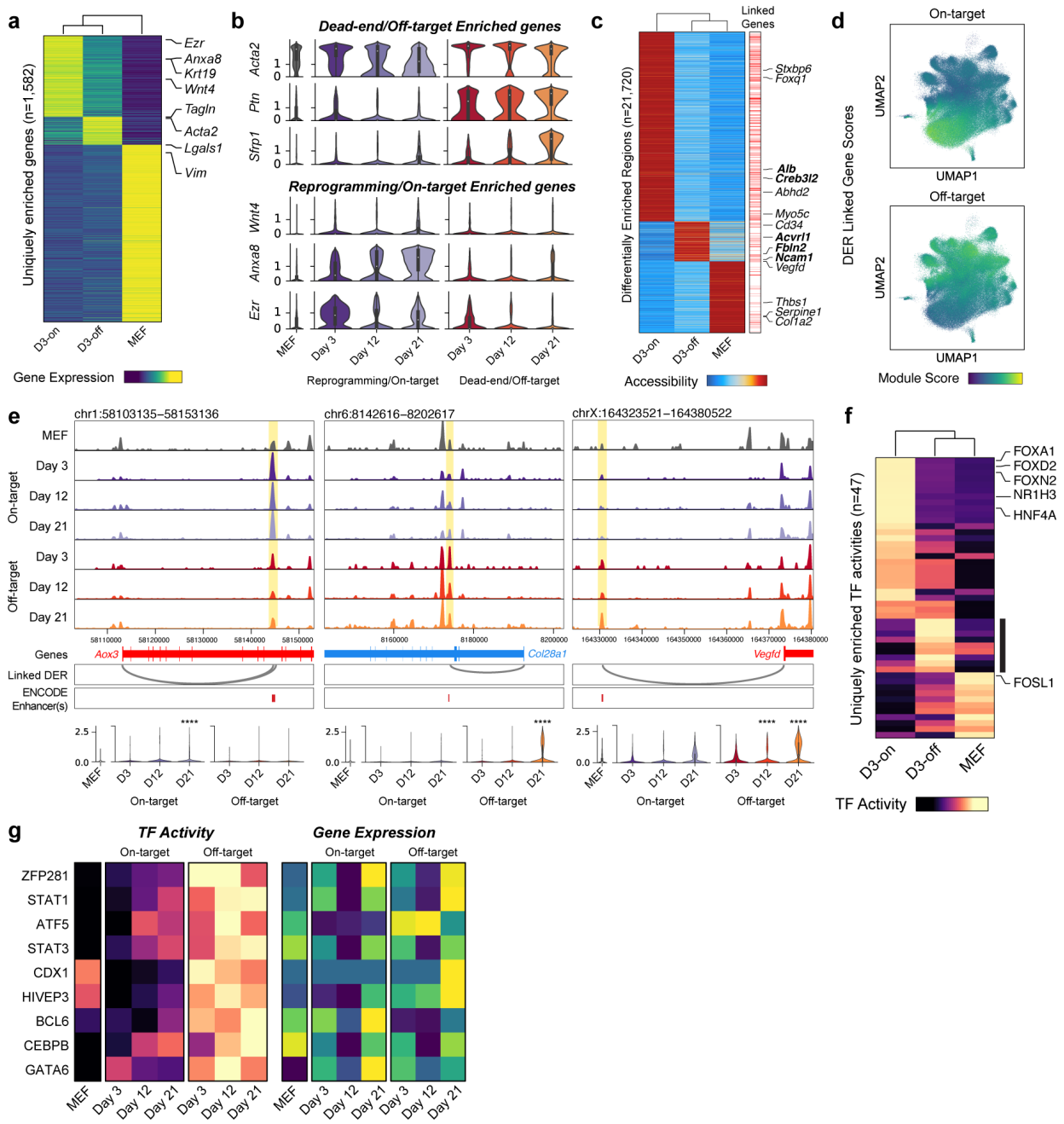

Figure 4. Assessing fate-specific changes in early cell state. (**a**) Heatmap of genes uniquely enriched across uninduced MEFs or one of the two reprogramming fates on Day 3 (FDR threshold: 0.05, log fold change threshold: 0). (**b**) Violin plots of several genes enriched in either off-target (dead-end) destined or on-target (reprogramming) destined cells. (**c**) Heatmap of peaks uniquely enriched across uninduced MEFs or one of the two reprogramming fates on Day 3 (FDR

625 threshold: 0.05, log fold change threshold: 1). Right panel shows annotation of peaks linked to
626 genes (Methods). (**d**) Module scores for genes linked to either on-target or off-target DERs
627 projected onto the clone-cell embedding. (**e**) Top panel: Accessibility browser tracks for each
628 lineage split by day, highlighting peaks linked to late lineage markers (On-target: *Aox3*; Off-target:
629 *Col28a1* and *Vegfd*) showing lineage specific changes in accessibility on Day 3. The *Aox3* and
630 *Vegfd* linked DERs overlap perfectly with an ENCODE enhancer like element (ELS) while the
631 *Col28a1* linked DER is within 100 bp of an ELS. Bottom panel: Expression levels of the three
632 genes across MEFs and the two reprogramming lineages split by days. The asterisks (*) mark
633 time points and lineage of significant differential enrichment. (**f**) Heatmap of TF activities uniquely
634 enriched across uninduced MEFs or one of the two reprogramming fates on Day 3 (FDR
635 threshold: 0.05, mean difference threshold: 0.5). (**g**) Left Panel: Heatmap showing TF activity (left
636 panel) and gene expression (right panel) levels for off-target associated TFs in MEFs and each
637 reprogramming lineage split by time points. TF activity signatures show a much stronger lineage
638 bias as compared to gene expression values.

Figure 5

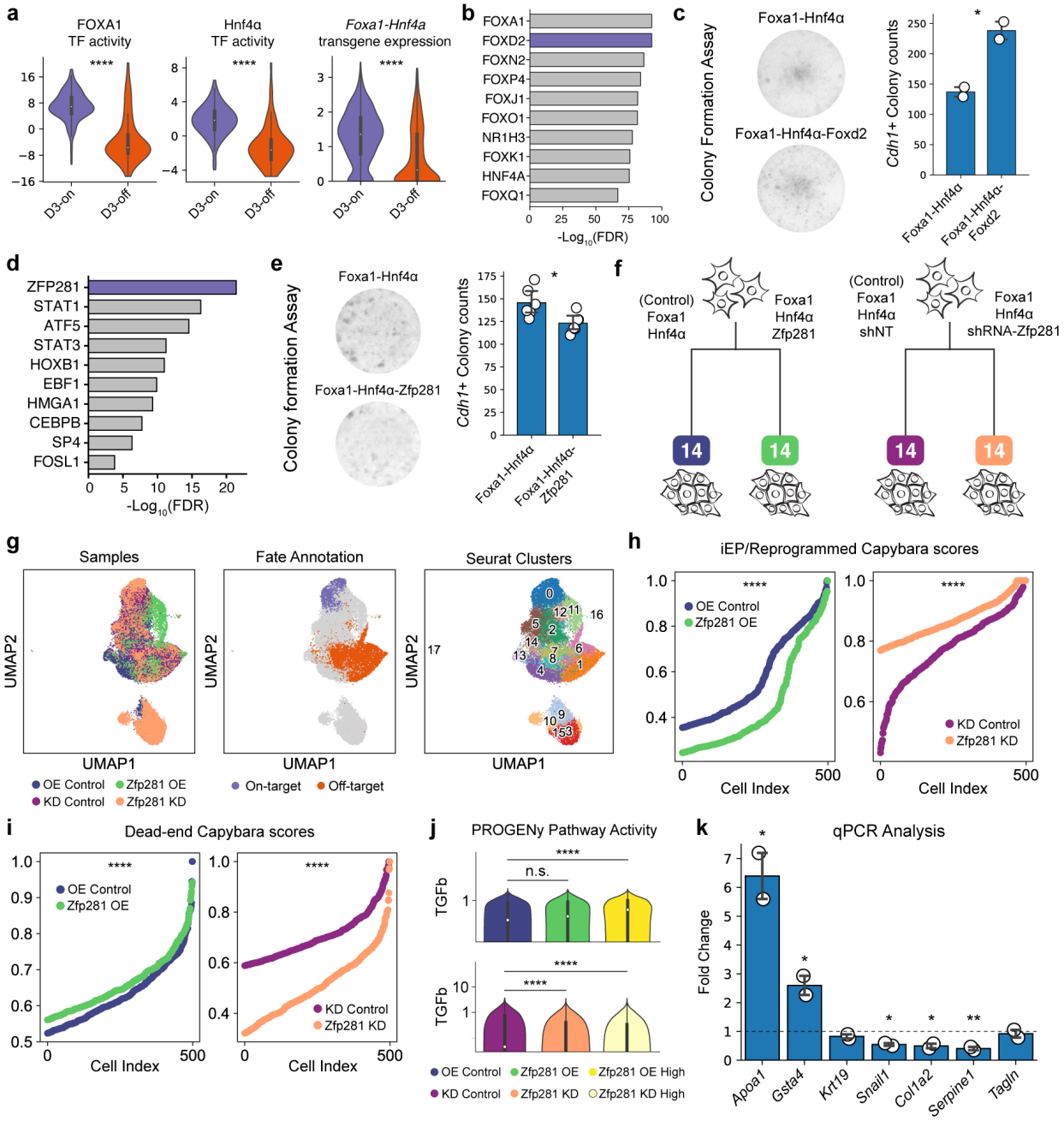

Figure 5. Identification of TF regulators of on-target and off-target reprogramming fate. (**a**) Left and Middle panels: Violin plots comparing enrichment of FOXA1 and HNF4A TF activities across the two reprogramming fates on Day 3 (Mann Whitney Wilcoxon test; p-values: FOXA1 = 9.2e-22, HNF4A = 1.7e-20). Right panel: Violin plot comparing enrichment of the *Hnf4α-Foxa1* transgene expression across the two reprogramming fates on Day 3 (Mann Whitney Wilcoxon

test; p-value = 6.5e-42). (**b**) Top ten TFs enriched in on-target destined cells based on TF activity scores. (**c**) Left Panel: Representative images from the *Foxd2* overexpression colony formation assay; Right Panel: Bar plot showing increase in CDH1-positive colony counts in *Foxd2* overexpressing cells compared to a standard reprogramming experiment (t-test; p-value = 0.045; n = 2 biological replicates). (**d**) Top ten TFs enriched in off-target destined cells based on TF activity scores. (**e**) Left Panel: Representative images from the *Zfp281* overexpression colony formation assay; Right Panel: Bar plot showing decrease in CDH1-positive colony counts in the *Zfp281* overexpressing sample compared to a standard reprogramming experiment. (t-test; p-value = 0.017; n = 6 biological replicates). (**f**) Schematic of the scRNA-seq experiment for *Zfp281* over-expression (OE) and knockdown (KD) during reprogramming. A GFP expression vector and non-target shRNA were used as controls for OE and KD respectively. (**g**) UMAP embedding for all cells profiled in the *Zfp281* OE and KD experiments with sample information (Left), cell fate annotation (Middle) and Seurat cluster information (Right) projected. (**h**) Plot of iEP Capybara identity scores across the KD and OE samples compared to respective controls (Mann Whitney Wilcoxon test; p-values: *Zfp281* OE vs control = 1.07e-53; *Zfp281* KD vs control = 2.19e-53). (**i**) Plot of dead-end Capybara identity scores across the KD and OE samples compared to respective controls (Mann Whitney Wilcoxon test; p-values: *Zfp281* OE vs control = 1.11e-11; *Zfp281* KD vs control = 3.26e-120). (**j**) Violin plots showing variation of TGF-β pathway activity across control vs OE vs OE high cells (upper panel) and control vs KD vs KD high cells (lower panel). OE high cells are defined as the subset OE sample cells with above average *Zfp281* expression. KD high cells are defined as the subset of KD sample cells with below average *Zfp281* expression. (**k**) Bar plots showing fold-change in reprogramming and dead-end marker genes upon small molecule mediated inhibition of TGF-β signaling, compared to a vehicle control, on Day 5 of iEP reprogramming (t-test; p-values: *Apoa1* = 0.02, *Col1a2* = 0.02, *Gsta4* = 0.04, *Serpine1* = 0.009, *Snail1* = 0.01; n=2 technical replicates).

680 **Methods**

681 **Tissue culture**

682 **Isolation of mouse LSK cells.** Lin$^-$ Sca1$^+$ c-Kit$^+$ (LSK) cells were obtained using a previously
683 described protocol[13]. Adult mice were euthanized, bone marrow was extracted from long bone,
684 hips and spine and passed through a 70µm filter. Cells were centrifuged at 300g for 10mins at 4C
685 and the pellet was resuspended in EasySep buffer (STEMCELL, Cat. 20144) at 100 million
686 cells/ml. EasySep lineage depletion kit (STEMCELL, Cat. 19856) was used to remove
687 differentiated cells. Finally, cells were stained for Sca1 (Sca1-AF488; BioLegend clone D7) and
688 cKit (CD117-PE; BioLegend clone 2B8) and sorted using the MoFlo Cell Sorter (Beckman
689 Coulter) with a 130µm nozzle. Isolated LSK cells were counted and used directly for lineage
690 tracing experiments.

691

692 **Mice and derivation of mouse embryonic fibroblasts.** MEFs were derived as previously
693 described[7]. Heads and visceral organs were removed from embryonic day (E)13.5 C57BL/6J
694 embryos (The Jackson laboratory: 000664) and the remaining tissue was minced with a razor
695 blade and then dissociated in a mixture of 0.05% trypsin and 0.25% collagenase IV (Life
696 Technologies) at 37 °C for 15 min. After passing the cell slurry through a 70-µM filter to remove
697 debris, cells were washed and then plated on 0.1% gelatin-coated plates, in DMEM supplemented
698 with 10% FBS (Gibco), 2mM l-glutamine and 50mM β-mercaptoethanol (Life Technologies). All
699 animal procedures were based on animal care guidelines approved by the Institutional Animal
700 Care and Use Committee.

701

702 **General Experimental methods**

703 **Lenti- and retro-virus production.** Lentiviral particles were produced by transfecting 293T-17
704 cells (ATCC: CRL-11268) with the pSMAL-CellTag-multi plasmid library, along with packaging
705 plasmids pCMV-VSVG (Addgene: 8454) and pCMV-dR8.2 dvpr (Addgene: 8455). Plasmids were
706 titered on 293T cells by serial dilution. Hnf4α-T2A-Foxa1 was cloned into the pGCDN-Sam
707 retroviral construct and packaged with pCL-Eco (Novus Biologicals: NBP2-29540), titered on
708 mouse fibroblasts. Virus was collected 48 hours and 72 hours after transfection and applied to
709 cells immediately following filtering through a low-protein binding 0.45-µm filter. Wherever
710 applicable, lentivirus was concentrated using high-speed centrifugation. 20ml of filtered viral
711 supernatant was centrifuged at 50,000g for 2.5 hours at 4ºC, supernatant was removed and the
712 virus was resuspended in 100ul of DMEM. The concentrated virus was stored at -80C.

713

714 **scRNA-seq library preparation.** 3' single-cell RNA library preparation was performed using the
715 Chromium Single Cell Gene Expression Kit from 10x Genomics. Cells were obtained as single-
716 cell suspensions and processed according to the manufacturer's instructions (CG000315).
717
718 **CellTag amplification for scRNA-seq (CellTag-RNA PCR).** An additional PCR step was used
719 to amplify CellTag barcodes from the single-cell cDNA library, obtained after step 2.4 of the 10x
720 Genomics Single Cell Gene Expression Kit user guide (CG000315). 5ul (or at least 60ng) of cDNA
721 was mixed with 2x Q5 HF PCR Master Mix (New England Biolabs) and 500nM of *P5/R1-par* and
722 *P7/SI-R2* primers in a 50ul reaction volume and subjected to the following PCR program: 98 C for
723 30 seconds; N cycles (98ºC for 10 seconds; 54ºC for 30 seconds; 72ºC for 30 seconds); 72ºC for
724 2 minutes. The number of PCR cycles (N) was kept the same as the number of cycles used during
725 sample index PCR of the main scRNA-seq library. CellTag amplicon library was purified using
726 double-sided bead purification (0.4x-0.64x) and quantified on an Agilent TapeStation using the
727 D1000-HS tape. Libraries were either sequenced by themselves (with a 50% Phi-X spike-in) or
728 along with scRNA-seq libraries (preferred). CellTag amplicon libraries were sequenced on an
729 Illumina NextSeq-500 to avoid index hopping-related artifacts. Primer sequences are available in
730 Supplementary Table 1.
731
732 **scATAC-seq library preparation.** Standard scATAC-seq library preparation was performed
733 using the Chromium Single Cell ATAC Kit from 10x Genomics. Cells were obtained as single-cell
734 suspensions, nuclei were isolated using 10x Genomics nuclei isolation protocol (CG000169), and
735 libraries were prepared according to the manufacturer's instructions (CG000209).
736
737 **scATAC-seq library preparation with modifications for CellTag capture.** To prepare single-
738 cell ATAC libraries with CellTag capture, nuclei were isolated using manufacturer's instructions
739 (CG000169; with the addition of an RNase inhibitor – Sigma 3335399001), centrifuged to remove
740 supernatant, and lightly fixed in 100ul 0.1% formaldehyde solution for 5 minutes. The reaction
741 was stopped for 5 minutes by adding 30ul of stop buffer (0.625M Glycine, 0.5% BSA, 0.25M ph8
742 Tris-Cl in PBS). The nuclei suspension was diluted using 100ul diluted nuclei buffer (10x
743 Genomics; CG000169) and pelleted using centrifugation. The pellet was subjected to
744 tagmentation for 60 minutes after re-suspension in a 15ul tagmentation reaction (for up to 15k
745 nuclei) according to the manufacturer's instructions (CG000209). After tagmentation, the reaction
746 mixture was diluted with 100ul dilute nuclei buffer, nuclei were pelleted using centrifugation and
747 subjected to targeted in situ reverse transcription in a 100ul reaction volume (20ul of 5x

748 SuperScript IV reaction buffer, 5ul each of dNTPs, DTT, RnaseOUT RNase inhibitor, SuperScript
749 IV Reverse Transcriptase, 1uM of primer *ctac2-rt1*) using the following temperature program: 4ºC
750 for 2 minutes; 10ºC for 2 minutes; 20ºC for 2 minutes; 30ºC for 2 minutes; 40ºC for 2 minutes;
751 45ºC for 10 minutes. After isRT, the reaction mixture was diluted with 100ul dilute nuclei buffer
752 and pelleted using centrifugation. 15ul GEM-nuclei mix was prepared to load nuclei on 10x
753 Genomics Chip E/H by mixing up to 15k nuclei with 6ul of ATAC buffer (from the 10x Genomics
754 scATAC-seq kit) and 3ul of 4uM primer *ctac2-rt1*. Any remaining volume was made up with dilute
755 nuclei buffer. GEM-nuclei mix was loaded onto Chip E/H along with ATAC GEM beads and
756 barcoding enzyme mix, the remaining steps of the scATAC-seq library preparation protocol were
757 performed according to the manufacturer's instructions. Primer sequences are available in
758 Supplementary Table 1. All centrifugation steps were performed at 500g for 10 minutes at 4ºC
759 unless stated otherwise.
760
761 **CellTag amplification for scATAC-seq (CellTag-ATAC PCR).** While CellTags can be recovered
762 directly from the sequenced scATAC-seq library with our library preparation, a higher yield can
763 be obtained using an additional targeted PCR step, similar to the scRNA-seq version. For this,
764 5ul of the library is collected after step 3.2 of the user guide (CG000209) and mixed with 2x Q5
765 HF master mix, 500nM of primer *biot-atac2_lin* and water in a 50ul reaction volume, and CellTag
766 containing fragments are linearly amplified using the following PCR program: 98ºC for 30
767 seconds; 20 cycles (98ºC for 10 seconds; 67ºC for 30 seconds; 72ºC for 30 seconds); 72ºC for 2
768 minutes. The CellTag amplicons are purified using streptavidin-coated magnetic bead pulldown
769 (ThermoFisher Scientific; Dynabeads™ MyOne™ Streptavidin C1) and purified fragments are
770 resuspended in 20ul of water. A final sample index PCR is performed to create a sequencible
771 library in presence of 2x Q5 master mix, 500nM each of *partial_p5* and *biot-atac2_e-rev* primers
772 in a 100ul reaction volume using the following PCR program: 98ºC for 30 seconds; 13 cycles
773 (98ºC for 10 seconds; 67ºC for 30 seconds; 72ºC for 30 seconds); 72ºC for 2 minutes and libraries
774 are purified using a double-sided bead cleanup, as described in Step 4.2 of 10x Genomic
775 scATAC-seq user guide (CG000209). Primer sequences are available in Supplementary Table 1.
776
777 **General Computational methods**
778 **Identifying clones.** Clone identification was performed based on our previously described
779 method[7,15]. Reads matching the CellTag-multi barcode sequence pattern
780 $(N)_3GT(N)_3CT(N)_3AG(N)_3TG(N)_3CA(N)_3$ were extracted from single-cell bam files as obtained
781 from CellRanger, filtered to remove false positive transcriptomic/genomic reads and reads

originating from non-cell droplets. For scRNA-seq, cell barcode-CellTag-UMI triplets represented by only a single read were discarded. We also provide an estimate of CellTag sequencing saturation to guide users if they require deeper sequencing of their CellTag libraries. CellTags were error-corrected using Starcode[73] to mitigate PCR/sequencing errors and filtered to remove sequences outside of the allowlist. Cell x CellTag read count (ATAC)/ UMI count (RNA) matrices were obtained, binarized and cells with too few or too many tags were removed to obtain the final Cell x CellTag matrices for scRNA-seq and scATAC-seq assays. Cell-cell similarity was computed using the Jaccard similarity metric and clones were identified using graph clustering. Whenever applicable, scRNA-seq and scATAC-seq CellTag matrices were merged before the Jaccard similarity calculation step, to identify clones across single-cell modalities. A detailed pipeline for clone calling can be found at: https://github.com/morris-lab/newCloneCalling

Clone cell embedding. To jointly visualize cells and clones on a single embedding, we developed a unique clone-cell graph embedding approach wherein we impute a cell-cell similarity graph with abstract clone nodes and use it as an input for graph embedding algorithms such as UMAP. For clone-cell embedding, we first obtained our single-cell data as an AnnData object and computed a cell-cell connectivity matrix based on PCA (in case of scRNA-seq) or CCA (in case of joint scRNA-seq scATAC-seq embedding). Next, we created a new AnnData object containing both cells and clones as observations. The connectivity matrix in the .obsm['connectivities'] slot was expanded to introduce clones. Then, clones were connected to their constituent cells by setting the respective entries in the expanded 'connectivities' matrix to 1. Finally, we used this clone-cell AnnData object with the expanded connectivity matrix as an input to graph embedding algorithms such as UMAP or Force Atlas.

Section 1

CellTag-multi library synthesis. CellTag-multi library was synthesized using Restriction Free (RF) cloning[74]. CellTag-multi barcodes were obtained as a gBlock from IDT DNA (see Supplementary Table 1 for sequence) and cloned into the pSMAL-ctac2 vector. 20ng of the CellTag-multi-v1 gBlock and 100ng of pSMAL-ctac2 vector were mixed with 2x Phusion PCR master mix in a 20ul reaction volume. The reaction mixture was subjected to the following thermal cycling program: 98ºC for 30 seconds; 15 cycles (98ºC for 8 seconds, 60ºC for 20 seconds, and 72ºC for 4.5 minutes); 72ºC for 5 minutes. The parental plasmid was digested by adding 2ul of methylation-sensitive restriction enzyme, *DpnI* (New England Biolabs), and incubating the reaction at 37ºC for 2 hours followed by inactivation at 80ºC for 20 minutes. 10ul of the reaction

816 mix was transformed directly into 100ul of Stellar chemically competent cells (Takara Bio), cells
817 were allowed to recover at 37ºC, 250rpm in 1ml of SOC media and plated on a Nunc Square
818 BioAssay plate (Cat. 166508). Plates were incubated overnight at 37ºC. Bacterial colonies were
819 collected using a scraper and allowed to recover in 150ml of LB media supplemented with
820 100ug/ml Ampicillin. CellTag-multi libraries were purified using a Qiagen High speed maxi prep
821 kit (Cat. 12662) and library complexity was assessed as described below. This cloning was
822 performed four times and libraries from each round were pooled to obtain the final high complexity
823 library.
824
825 **Assessing the complexity of CellTag-multi libraries and allowlisting.** A list of allowed CellTag
826 sequences for each CellTag library was created using amplicon sequencing. 50ng of CellTag
827 plasmid library was mixed with 2x Q5 HF Master Mix, 2.5ul each of 0.5uM primers *bATAC_fwd*
828 and *bATAC_rev* in a 25ul reaction volume and subjected to the following PCR program: 98ºC for
829 30 seconds; 10 cycles (98ºC for 10 seconds; 63ºC for 30 seconds; 72ºC for 1 minute). Two
830 amplicon libraries were generated from each CellTag library plasmid preparation in parallel and
831 sequenced on an Illumina Miseq. For each replicate, reads matching the CellTag sequence
832 pattern $(N)_3GT(N)_3CT(N)_3AG(N)_3TG(N)_3CA(N)_3$ were extracted, sequencing/PCR errors were
833 corrected by collapsing tags within 4 edits of each other using starcode[73] and thresholded to retain
834 CellTags containing at least N reads where N = max(10, 90th percentile/10). An allowlist was
835 created by collecting all CellTag sequences retained in thresholded lists from both replicates.
836 Allowlists from the four CellTag libraries were combined to create the master allowlist for the
837 CellTag-multi library (Supplementary Table 2). The detailed analysis code can be found at:
838 https://github.com/morris-lab/newCloneCalling
839
840 **Species mixing experiment**. For the species mixing experiment, mouse iEP-LT cells were
841 tagged with CellTag-multi-v1 library, containing the barcode pattern
842 $(N)_3GT(N)_3CT(N)_3AG(N)_3TG(N)_3CA(N)_3$ and human HEK 293T cells with CellTag-multi-v0 library,
843 containing the barcode pattern $(N)_5GTA(N)_5CCT(N)_5ATC(N)_5GAT(N)_5$. Nuclei were isolated from
844 both species using the Nuclei Isolation for scATAC-seq protocol from 10x Genomics (CG000169)
845 and mixed in a 1:1 ratio. The mixed nuclei sample was processed using the standard scATAC-
846 seq library preparation protocol (v1 kit) from 10x Genomics with modifications to capture CellTags.
847 Single-cell libraries were sequenced on an Illumina Nextseq-500. The resulting sequencing data
848 was aligned to a mixed species reference using CellTag-ATAC v1. The aligned bam file was used
849 for downstream analysis.

850 Reads matching v0 or v1 CellTags were parsed from the mixed species single-cell aligned
851 bam file. Each cell barcode was assigned to one of four categories, based on CellRanger-ATAC
852 species assignments - human, mouse, doublet, non-cell; the distribution of v0 and v1 reads was
853 assessed across the four categories. Cells with fewer than two CellTag reads across both libraries
854 were discarded and the remaining cells were plotted on a barnyard plot. We quantified inter-
855 species cross-talk of CellTags, by calculating the percent of cells, with at least 2 CellTag
856 reads/cell, having less than 95% of CellTag reads originating from the correct, species-specific
857 CellTag library.
858
859 **Assessing the effect of isRT on chromatin accessibility signal.** We compared the effect of
860 introducing an isRT step on scATAC-seq data quality. For this, two single-cell ATAC libraries were
861 prepared with CellTagged HEK 293T cells using either the original 10x Genomics scATAC library
862 preparation protocol (Original) or our modified method (Modified). Sequencing data from both was
863 processed with ArchR[75], dimensionally reduced using LSI, clustered using Louvain clustering, and
864 peaks were identified across samples. Both datasets were compared across several standard
865 scATAC-seq data quality metrics such as fragment size distribution, TSS scores, the number of
866 unique fragments per cell and Fraction reads in Peaks (FRiP) per cell. To compare genome-wide
867 accessibility data across samples, normalized peak counts (Counts Per Million; CPM) were
868 calculated for each sample and plotted on a scatter plot and the Pearson Correlation coefficient
869 was calculated to quantify the similarity between the accessibility signal of the two samples.
870
871 **Analysis of clones in expanded reprogramming fibroblasts.** A subset of the data obtained
872 from our reprogramming dataset (described in section 3) from Days 12 and 21 was used for this
873 analysis. Clones were identified following the standard computational workflow as described
874 above. CellTag abundance was calculated for each CellTag as the percent of metric filtered cells
875 containing that CellTag. Browser tracks depicting single-cell accessibility fragments were plotted
876 using ArchR. Gene expression and gene scores values were averaged on a clonal level.
877 Spearman correlation coefficients were calculated between clonal gene expression and gene
878 score both within (Intra clonal) and across clones (Inter clonal).
879
880 **Section 2**
881 **Lineage tracing during in vitro mouse hematopoiesis.** LSK cells were purified as described
882 above, counted and 5,500 cells were added to a 96-well U-bottom suspension culture plate
883 (GenClone Cat. 25-224) and allowed to recover in broad myeloid differentiation media[13] consisting

884 of SFEM media (STEMCELL), Pen/Strep, IL-3 (20ng/mL; PeproTech Cat. 213-13), FLT3-L
885 (50ng/mL; PeproTech Cat. 250-31L), IL-11 (50ng/mL; PeproTech Cat. 220-11), IL-5 (10ng/mL;
886 PeproTech Cat. 215-15), EPO (3U/mL; PeproTech Cat. 100-64), TPO (50ng/mL; PeproTech Cat.
887 315-14), and mSCF (50ng/mL; R&D Systems Cat. Q78ED8) and IL-6 (10ng/mL; R&D Systems
888 Cat. 406-ML-005) at 37ºC for 2 hours.
889 To allow clone tracking, cells were transduced for 2 days with 10ul of concentrated
890 CellTag-multi virus (~25k unique CellTag sequences) in 100ul differentiation media, in the
891 presence of 6ug/ml DEAE-Dextran after spin-fection at 800g for 90 minutes at 37ºC. 60 hours
892 (2.5 days) after the start of the experiment, 50% of the cells were collected for single-cell profiling
893 and split equally between scRNA-seq and scATAC-seq assays. The remaining cells were split
894 into 2 technical replicates and re-plated in fresh differentiation media. Finally, all the cells were
895 collected on Day 5 and split between scRNA-seq and scATAC-seq profiling.
896
897 **Single-cell library preparation and sequencing.** The v3 single index Gene Expression kit and
898 the v1 scATAC kit from 10x Genomics were used for single-cell library preparation. CellTag-RNA
899 PCR was used to obtain CellTag amplicon libraries as described above. scRNA-seq libraries were
900 sequenced on an Illumina NovaSeq-6000 and the resulting data was computationally dehopped.
901 CellTag amplicon libraries obtained from scRNA-seq libraries were sequenced on an Illumina
902 NextSeq-500. For read alignment, CellTag and transcriptome read files for each sample were
903 processed together using CellRanger, using a custom mm10 reference containing the GFP CDS
904 and UTR, to produce one aligned bam file per sample. scATAC-seq libraries containing both
905 accessible chromatin and CellTag fragments were sequenced on an Illumina NextSeq-500 and
906 processed using CellRanger-ATAC, using the default mm10 reference genome. Aligned bam files
907 from both modalities were used for CellTag processing, other CellRanger and CellRanger-ATAC
908 outputs were used for downstream single-cell analyses.
909
910 **Basic single-cell and clonal analysis of the Hematopoiesis dataset.** CellRanger generated
911 scRNA-seq count matrices were processed using Seurat. Low-quality cells with high
912 mitochondrial reads, low UMIs, and features per cell were removed. Day 2.5 and Day 5 samples
913 were integrated using SCTransform, dimensionally reduced using PCA, and clustered using
914 Louvain clustering. scRNA-seq clusters were annotated using marker gene expression.
915 Fragments files from scATAC-seq samples were processed using ArchR v1.0.1. Valid cell
916 barcodes, as identified by CellRanger-ATAC and passing default ArchR quality filters were
917 retained. Cells were dimensionally reduced using iterative LSI and clustered using Louvain

clustering. Cell type labels were transferred to scATAC-seq clusters using Seurat label transfer and annotations were manually inspected using marker gene scores. For RNA-ATAC co-embedding, scRNA-seq gene expression matrix and scATAC-seq MAGIC imputed[76] Gene Score matrix, as obtained from ArchR, were used as input to the RunCCA function in Seurat. A union set of the top 5000 highly variable genes from each dataset were used for this co-embedding.

For clone calling, reads mapping to the CellTag barcode were extracted from single-cell aligned bam files as obtained from CellRanger and CellRanger-ATAC. CellTag data within each modality was merged, retaining sample-of-origin information in the cell barcode, and cell x CellTag UMI (for RNA) and read (for ATAC) count matrices were obtained for each modality. The RNA matrix was binarized at a threshold of more than one UMI count and cells with 2 to 25 CellTags were retained. The ATAC matrix was binarized at a threshold of more than one read count and cells with 1 to 25 CellTags were retained. The two filtered matrices were merged, cell-cell Jaccard similarity matrix was computed and thresholded at 0.6 (for cell pairs within the same modality) and 0.5 (for cell pairs across modalities). The final thresholded matrix was used to identify clones across the entire dataset. Clone-cell embedding was computed as described above, and ForceAtlas2 was used to jointly visualize clones and cells. This embedding was also generated separately for sub-clones where clones were split either by modality or by both, time point and modality.

State-fate linkage in hematopoiesis. To link cell state with fate, we first obtained all clones spanning the two time points (state-fate clones). Each state-fate clone was assigned a fate label, which was the most common fate amongst its Day 5 sisters. Less common lineages were grouped based on similarity, e.g. Erythroid and Megakaryocytes (Ery/Meg); Eosinophils, Basophils, and Mast Cells (Baso/Eos/Mast). Ccr7 DCs and plastoid DCs (DCs). Clones annotated to transition/ progenitor fates were excluded from state-fate analysis unless otherwise specified. Fate bias scores were calculated as percent of Day 5 fate sisters belonging to the annotated fate label.

To map Day 2.5 (state) sub-clones on the clone-cell embedding, we split each clone into sub-clones based on the time point of collection and assay of each sister, to obtain up to four sub-clones RNA/ATAC – state/fate sub-clones. The clone-cell embedding was recomputed using these sub-clones. Overlap between RNA and ATAC sub-clones across the two single-cell modalities was calculated within each ‘fate potential’ group using the Wasserstein distance metric computed with a 30-dimensional embedding of the sub-clone nodes obtained using the UMAP algorithm. To quantify if state sub-clones closer to the periphery of a 'fate potential’ group were less fate biased, we devised a closeness metric, which is the minimum distance of a state sub-

clone from the centroid of an alternative fate potential group. A higher closeness metric would mean that a state sub-clone is farther away from centroids of other fate potential groups. The relationship between the closeness metric and fate bias was plotted using a percentile plot, with percentile rank for the closeness metric on the X-axis and mean fate bias scores for state sub-clones passing the percentile rank on the Y-axis.

To characterize functional priming of cell state, Day 2.5 state sisters in each fate potential group were compared to the rest in gene expression and TF activity space. For scRNA-seq features, we used residuals obtained for the top 3000 highly variable genes after SCTransform normalization in Seurat. For scATAC-seq features, we used TF activity z-scores obtained from chromVAR using the default mouse motif set in ArchR (884 TF motifs). Correction for multiple hypothesis testing was performed using the Benjamini-Hochberg method, setting the FDR threshold for significance at 0.05, unless otherwise specified.

Fate prediction from cell state using machine learning. State-fate machine learning was performed to quantify the predictability of cell fate from early state. A machine learning classifier was tasked to predict the discrete clonal fate label Y as obtained above (possible fate labels: ‘progenitor’, ‘monocyte’, ‘neutrophil’, ‘Lym/pDC/Ccr7-DC’, ‘Ery/Meg’ or ‘Baso/Eos/Mast’), from an input vector of single-cell features X of Day 2.5 cells. For RNA only model, we used residuals of the top 3000 genes for input, for ATAC only model, we used TF activity z-scores (with k-nn imputation where k=20) as input and for the RNA+ATAC model, we randomly paired RNA and ATAC cells within the same sub-clone and concatenated their respective RNA and ATAC feature vectors and used those as input. For training, we used the Repeated Stratified k-fold cross-validation procedure setting both *n_splits* and *n_repeats* to 5. Model performance was evaluated using accuracy and Weighted F1 score.

For each machine learning task, we tested a panel of classifier architectures, logistic regression, LightGBM, and Random Forest. Each was trained and evaluated using the procedure described above. Hyperparameter tuning was performed for each and the following values were tested:

- Random Forest: n_estimators: [100, 300, 1000], max_depth: [10, 50, None], min_samples_leaf: [1, 2, 4], bootstrap: [True, False]
- LightGBM: num_leaves: [7,15,31,80], max_depth: [5,9,30], min_data_in_leaf: [20, 40, 80], bagging_fraction: [0.8,1], bagging_freq: [3], feature_fraction: [0.1, 0.9]
- Logistic Regression: penalty: ['l2', 'none'], C: np.logspace(-4, 4, 20), solver: ['lbfgs','newton-cg','saga'], max_iter: [1000]

986 The python library 'scikit-learn' was used for all machine learning analysis.
987
988 **Fate prediction using TF activities derived from distal, intronic, exonic, and promoter peak**
989 **sets.** ATAC peaks were categorized as intronic, exonic, promoter, or distal using default ArchR
990 definitions. TF activity scores were calculated for each peak set independently and used for state-
991 fate prediction analysis as described above. To test if variation in model performance was due to
992 different numbers of peaks in each set, all peak sets were randomly sub-sampled to 8823 peaks
993 (number of peaks in the exonic set), TF activity scores were calculated again and state-fate
994 prediction was performed using these new scores.
995
996 **SHapley Additive exPlanations (SHAP) analysis.** The shap python package was used to
997 perform SHAP analysis and interpret trained machine learning models. The TreeExplainer
998 function from the 'shap' python package was used to calculate SHAP values for trained random
999 forest models. For each input feature and fate label, SHAP values were calculated using each
1000 data point in the 25 test sets (*n_splits* x *n_repeats*), resulting in 5 SHAP values per data point per
1001 feature. This helped average out any rare outlier values generated due to a model training artifact.
1002 Feature importance scores were calculated for each input feature for the prediction of each fate
1003 label, by taking the mean of absolute SHAP values for each feature-fate combination. To identify
1004 features positively or negatively correlated with the prediction of a fate label, SHAP correlation
1005 was performed. For each input feature, the Pearson correlation coefficient between its values
1006 (expression/TF activity) and its SHAP values for a given fate was calculated, resulting in one
1007 correlation value per feature per fate.
1008
1009 **Section 3**
1010 **Lineage tracing during iEP reprogramming.** Cryo-preserved P0 MEFs were thawed and
1011 seeded in 0.1% gelatin-coated six-well plates, in DMEM supplemented with 10% FBS, 2 mM l-
1012 glutamine, and 50 mM β-mercaptoethanol (Life Technologies) and penicillin-streptomycin at a
1013 density of 30,000 cells/well. After overnight recovery at 37ºC, cells were transduced every 12
1014 hours for 2 days, with fresh Hnf4α-T2A-Foxa1 retrovirus in the presence of 4 µg/ml protamine
1015 sulfate (Sigma-Aldrich). During the last round of transduction, the retroviral mix was supplemented
1016 with CellTag-multi lentiviral library to initiate clone tracking. On Day 0 of reprogramming, cell
1017 culture media was changed to hepato-medium (DMEM:F-12, supplemented with 10% FBS, 1
1018 µg/ml insulin (Sigma-Aldrich), 100 nM dexamethasone (Sigma-Aldrich), 10 mM nicotinamide
1019 (Sigma-Aldrich), 2 mM l-glutamine, 50 mM β-mercaptoethanol (Life Technologies), and penicillin-

1020 streptomycin, containing 20 ng/ml epidermal growth factor (Sigma-Aldrich)). After 72 hours (Day
1021 3 of reprogramming), cells were dissociated, two-thirds of the cells were collected for single-cell
1022 sequencing and the remaining cells were re-plated on 6-well plates coated with 5 μg/cm^2 Type I
1023 rat collagen (Gibco, A1048301). Two additional samples were collected on Days 11 and 21 for
1024 single-cell sequencing. We used the 10x Genomics v3.1 dual index Gene Expression kit (PN-
1025 1000268) and the v1.1 ATAC kit (PN-1000175) for single-cell profiling. This experiment was
1026 performed in two biological replicates.
1027 CellTag PCR was performed for all scRNA-seq and scATAC-seq libraries, as described
1028 above. scRNA-seq and scATAC-seq libraries were sequenced on an Illumina NovaSeq-6000.
1029 CellTag amplicon libraries were sequenced on an Illumina NextSeq-500 to avoid any index
1030 hopping related artifacts. For read alignment, CellTag and transcriptome/chromatin read files for
1031 each sample were processed together using CellRanger/CellRanger-ATAC, to produce one
1032 aligned bam file per sample. Aligned bam files from both modalities were used for CellTag
1033 processing, other CellRanger and CellRanger-ATAC outputs were used for downstream single-
1034 cell analyses.
1035
1036 **Basic single-cell and clonal analysis of the direct reprogramming dataset.** scRNA-seq count
1037 matrices were processed using Seurat. Quality filtering was performed to remove cells with high
1038 mitochondrial reads and low UMIs and genes per cell. scRNA-seq samples across all time points
1039 and biological replicates were integrated, dimensionally reduced using PCA, and clustered using
1040 Louvain clustering. Cells from Days 12 and 21 were subsetted and re-clustered. Single-cell
1041 identity scores were obtained using Capybara, using Fibroblasts (MEFs), , and reprogrammed,
1042 and dead-end trajectories from a previous dataset[7] as references. Cell clusters were annotated
1043 as 'reprogrammed', 'dead-end', or 'transition' based on these cell identity scores and marker gene
1044 expression. Fragments files from scATAC-seq samples were processed using ArchR. Valid cell
1045 barcodes, as identified by CellRanger-ATAC and passing default ArchR quality filters were
1046 retained. Cells were dimensionally reduced using iterative LSI and clustered using Louvain
1047 clustering. Cells were annotated as 'reprogrammed', 'dead-end', or 'transition' based on marker
1048 gene accessibility. For RNA-ATAC co-embedding, scRNA-seq gene expression matrix and
1049 scATAC-seq MAGIC imputed[76] Gene Score matrix, as obtained from ArchR, were used as input
1050 to the RunCCA function in Seurat. A union set of the top 2000 highly variable genes from each
1051 dataset were used for this co-embedding.
1052 For clone calling, reads mapping to the CellTag barcode were extracted from single-cell
1053 aligned bam files as obtained from CellRanger and CellRanger-ATAC. CellTag data within each

1054 modality was merged, retaining sample-of-origin information in the cell barcode, and cell x CellTag
1055 UMI (for RNA) and read (for ATAC) count matrices were obtained for each modality. The RNA
1056 matrix was binarized at a threshold of more than one UMI count and cells with 2 to 25 CellTags
1057 were retained. The ATAC matrix was binarized at a threshold of more than one read count and
1058 cells with 2 to 25 CellTags were retained. The two filtered matrices were merged, cell-cell Jaccard
1059 similarity matrix was computed and thresholded at 0.6. The final thresholded matrix was used to
1060 identify clones across the entire dataset. Clone-cell embedding was computed as described
1061 above and the UMAP algorithm was used to jointly visualize clones and cells.
1062
1063 **State-fate analysis for the direct reprogramming dataset.** Clones were annotated with one of
1064 three fates – 'reprogrammed', 'transition', or 'dead-end', based on the most abundant cell type
1065 amongst fate sisters. Clonal fate bias scores were calculated as percent of fate sisters (Days 12
1066 and 21) belonging to the annotated fate label. Alluvial plots were constructed using the ggAlluvial
1067 R package. State-fate machine learning analysis was performed exactly as described in the
1068 hematopoiesis section. Classification models were trained to predict either 'reprogrammed' or
1069 'dead-end' fates. Since the frequency distribution of fate labels was less skewed for the
1070 reprogramming dataset, only prediction accuracy scores were used as performance metrics.
1071 CellRank analysis was performed for a 40,000-cell subset of the scRNA-seq dataset, due to
1072 scalability limitations. For feature enrichment analysis, Day 3 sisters in state-fate clones were
1073 grouped by fate. Seurat FindMarkers function was used to identify gene expression markers and
1074 ArchR getMarkerFeatures function was used to identify peak and TF activity markers for each of
1075 the following cell groups - uninduced MEFs, on-target destined cells and, off-target destined cells,
1076 in a series of one versus all comparisons. For peak and TF activity comparisons, both on-target
1077 and off-target cell groups were expanded using k-nearest neighbors (k=5). Uniquely enriched
1078 features (genes/peaks/TFs) were obtained by removing features that were identified as markers
1079 of more than one cell group. TF activity results were further refined by discarding TFs with low
1080 gene score-TF activity correlation (< 0.3). Motif enrichment analysis was performed using the
1081 HOMER package[77] for both on-target and off-target DERs using MEF DERs as background, to
1082 better resolve fate-specific motif enrichment. Mouse ENCODE ELS elements were obtained from
1083 the ENCODE SCREEN database[41]. Only genomic regions annotated as dELS, pELS, dELS,
1084 CTCF-bound, or pELS, CTCF-bound in the SCREEN database were used for enrichment
1085 analysis. The FigR[40] package was used for peak-to-gene linkage analysis. Optimal matching was
1086 used to pair RNA and ATAC cells from the same time points followed by the runGenePeakcorr
1087 function to identify peak-gene pairs. Peak-gene pairs with an adjusted p-value greater than or

1088 equal to 0.05 were discarded. *Foxa1* and *Hnf4α* ChIP-seq peaks from Day 2 of reprogramming
1089 were obtained[53]. These peak sets were added as custom annotations in ArchR and single-cell
1090 accessibility z-scores for each peak set were computed using the addDeviationsMatrix function
1091 in ArchR.
1092
1093 **Computational analysis related to ZFP281 motifs.** Tomtom analysis[56] from the MEME-ChIP
1094 package was used to find highly similar motifs to *Zfp281*. The *Zfp281* position frequency matrix
1095 (PFM) was obtained from ArchR and used as input to the Tomtom web interface. Highly correlated
1096 TF motifs with q-value less than 0.05 were obtained, these were further subsetted for TF activities
1097 enriched in off-target destined cells resulting in a total of four TF motifs for comparison with
1098 *Zfp281*. *Zfp281* ChIP-seq peaks were obtained[54] and single-cell accessibility z-scores were
1099 computed using the addDeviationsMatrix function in ArchR. *Zfp281* gene targets[57] were used as
1100 inputs for a state-fate prediction model, which was trained and evaluated as described above and
1101 compared to a sized-matched set of random genes.
1102
1103 **Plasmid cloning related to Foxd2 and Zfp281 experiments.** Non-targeting shRNA construct
1104 was obtained from Sigma (SHC202; pLKO.5-puro Control Plasmid). Zfp281 targeting shRNA
1105 gene was obtained from Sigma (Clone ID: TRCN0000255746) and cloned into the pLKO.5-puro
1106 lentiviral construct (Sigma SHC201). For over-expression, cDNA fragments were cloned in the
1107 pGCDNsam retroviral construct. *Zfp281* cDNA was obtained from OriGene (Cat. MC205914) and
1108 *Foxd2* cDNA was reverse transcribed from RNA obtained from long-term iEP cells.
1109
1110 **Reprogramming with Foxd2 and Zfp281 perturbations.** Reprogramming was performed as
1111 described above, with the following modifications. For over-expression, cells were transduced
1112 with a 1:1 mixture of *Foxd2/Zfp281* retrovirus and *Hnf4α-Foxa1* reprogramming retrovirus every
1113 12 hours for 2 days. Control cells were transduced with a 1:1 mixture of a GFP control retrovirus
1114 and *Hnf4α-Foxa1* reprogramming retrovirus for the same amount of time. For knockdown, cells
1115 were transduced with the non-targeting control/*Zfp281*-shRNA lentivirus every 12 hours for 1 day
1116 after the 2-day *Hnf4α-Foxa1* retroviral transduction was completed.
1117
1118 **Single-cell analysis for Foxd2 and Zfp281 experiments.** Dual indexed v3.1 scRNA-seq
1119 libraries were prepared for all four samples (*Zfp281* OE, OE Control, *Zfp281* KD, KD Control)
1120 according to the manufacturer's instructions (CG000315) and sequenced on a Nextseq-500.
1121 Count matrices were generated and integrated using CellRanger count and aggr commands and

1122 processed using Seurat. Quality filtering was performed to remove cells with high mitochondrial
1123 reads and low UMIs and genes per cell. Cells were dimensionally reduced using PCA, cell cycle
1124 regressed, clustered using Louvain clustering, and visualized using UMAP. Capybara identity
1125 scores were calculated as described in the iEP lineage tracing section above. Markers for each
1126 lineage across time points and uninduced MEFs were obtained (log2 fold change > 0.7, adjusted
1127 p-value < 0.05) and used for gene module scoring for all four samples. Cell clusters displaying
1128 strong enrichment of on-target or off-target markers were annotated with the respective fates.
1129 pROGENY pathway analysis[60] was used to calculate single-cell activity scores for the TGF-β
1130 signaling pathway.
1131
1132 **Colony formation assays.** Colony formation assays were performed as previously described[7].
1133 Reprogramming cells were seeded at low plating density in collagen-coated 6-well plates within
1134 the first 4 days and allowed to form colonies over 2 weeks of reprogramming. Following this, cells
1135 were fixed using 4% paraformaldehyde, permeabilized using 0.1% Triton-X and processed for
1136 CDH1 (E-Cadherin) staining using the VIP peroxidase substrate kit (Vector labs SK4600) and
1137 anti-mouse E-Cadherin primary antibody (1:100, BD Biosciences). Stained colonies were imaged
1138 using a flatbed scanner and quantified using the following script: https://github.com/morris-
1139 lab/Colony-counter
1140
1141 **Quantitative PCR and analysis.** Cells were collected for RNA extraction (RNeasy kit; QIAgen)
1142 on Day 12 of reprogramming and reverse transcribed using the Maxima RT kit (ThermoFisher
1143 K1672). 20ng of reverse transcribed RNA was mixed with TaqMan™ Gene Expression Master
1144 Mix (ThermoFisher Scientific) and gene-specific TaqMan™ probes (Supplementary Table 8) in a
1145 20ul reaction volume and processed according to manufacturer's instructions (4371135) on the
1146 StepOne Plus qPCR system. Per gene fold change for Foxd2 overexpressing cells was calculated
1147 relative to control reprogramming cells (*Hnf4α-Foxa1* and GFP control overexpression) that were
1148 processed in parallel, after normalization to the housekeeping gene, *Actb*.
1149
1150 **Reprogramming with TGF-β inhibition.** Cells were reprogrammed as described above. Cells
1151 were cultured in hepatic media supplemented with 2.6μM of SB431542 (STEM CELL 72232), a
1152 small molecule inhibitor of TGF-b signaling starting on Day 0 of reprogramming. SB431542
1153 containing media was changed every 2 days. Cells were collected for qPCR analysis on Day 5 of
1154 reprogramming and processed as described above.
1155

1156 **References**

1157 1. What Is Your Conceptual Definition of “Cell Type” in the Context of a Mature Organism?
1158 *Cell Syst.* **4**, 255–259 (2017).
1159 2. Stuart, T. & Satija, R. Integrative single-cell analysis. *Nat. Rev. Genet.* **20**, 257–272
1160 (2019).
1161 3. Morris, S. A. The evolving concept of cell identity in the single cell era. *Dev.* **146**, (2019).
1162 4. Kester, L. & van Oudenaarden, A. Single-Cell Transcriptomics Meets Lineage Tracing.
1163 *Cell Stem Cell* **23**, 166–179 (2018).
1164 5. VanHorn, S. & Morris, S. A. Next-Generation Lineage Tracing and Fate Mapping to
1165 Interrogate Development. *Developmental Cell* vol. 56 7–21 (2021).
1166 6. Alemany, A., Florescu, M., Baron, C. S., Peterson-Maduro, J. & van Oudenaarden, A.
1167 Whole-organism clone tracing using single-cell sequencing. *Nature* **556**, 108–112 (2018).
1168 7. Biddy, B. A. *et al.* Single-cell mapping of lineage and identity in direct reprogramming.
1169 *Nature* **564**, 219–224 (2018).
1170 8. Bowling, S. *et al.* An Engineered CRISPR-Cas9 Mouse Line for Simultaneous Readout of
1171 Lineage Histories and Gene Expression Profiles in Single Cells. *Cell* **181**, 1410-1422.e27
1172 (2020).
1173 9. Frieda, K. L. *et al.* Synthetic recording and in situ readout of lineage information in single
1174 cells. *Nature* **541**, 107–111 (2017).
1175 10. Raj, B. *et al.* Simultaneous single-cell profiling of lineages and cell types in the vertebrate
1176 brain. *Nat. Biotechnol.* **36**, 442–450 (2018).
1177 11. Spanjaard, B. *et al.* Simultaneous lineage tracing and cell-type identification using
1178 CRISPR–Cas9-induced genetic scars. *Nat. Biotechnol.* **36**, 469–473 (2018).
1179 12. Wagner, D. E. & Klein, A. M. Lineage tracing meets single-cell omics: opportunities and
1180 challenges. *Nat. Rev. Genet.* 1–18 (2020) doi:10.1038/s41576-020-0223-2.
1181 13. Weinreb, C., Rodriguez-Fraticelli, A., Camargo, F. D. & Klein, A. M. Lineage tracing on
1182 transcriptional landscapes links state to fate during differentiation. *Science (80-.).* **367**,
1183 (2020).
1184 14. Kester, L. & van Oudenaarden, A. Single-Cell Transcriptomics Meets Lineage Tracing.
1185 *Cell Stem Cell* **23**, 166–179 (2018).
1186 15. Kong, W. *et al.* CellTagging: combinatorial indexing to simultaneously map lineage and
1187 identity at single-cell resolution. *Nat. Protoc.* **15**, 750–772 (2020).
1188 16. Guo, C. *et al.* CellTag Indexing: Genetic barcode-based sample multiplexing for single-
1189 cell genomics. *Genome Biol.* **20**, 1–13 (2019).

1190 17. Stuart, T. *et al.* Comprehensive Integration of Single-Cell Data. *Cell* **177**, 1888-1902.e21
1191 (2019).
1192 18. McInnes, L., Healy, J. & Melville, J. UMAP: Uniform Manifold Approximation and
1193 Projection for Dimension Reduction. (2018) doi:10.48550/arxiv.1802.03426.
1194 19. Jacomy, M., Venturini, T., Heymann, S. & Bastian, M. ForceAtlas2, a Continuous Graph
1195 Layout Algorithm for Handy Network Visualization Designed for the Gephi Software.
1196 *PLoS One* **9**, e98679 (2014).
1197 20. Buenrostro, J. D. *et al.* Integrated Single-Cell Analysis Maps the Continuous Regulatory
1198 Landscape of Human Hematopoietic Differentiation. *Cell* **173**, 1535-1548.e16 (2018).
1199 21. Velten, L. *et al.* Human haematopoietic stem cell lineage commitment is a continuous
1200 process. *Nat. Cell Biol. 2017 194* **19**, 271–281 (2017).
1201 22. Liu, Z. *et al.* Fate Mapping via Ms4a3-Expression History Traces Monocyte-Derived Cells.
1202 *Cell* **178**, 1509-1525.e19 (2019).
1203 23. Tiedt, R., Schomber, T., Hao-Shen, H. & Skoda, R. C. Pf4-Cre transgenic mice allow the
1204 generation of lineage-restricted gene knockouts for studying megakaryocyte and platelet
1205 function in vivo. *Blood* **109**, 1503–1506 (2007).
1206 24. Zriwil, A. *et al.* Direct role of FLT3 in regulation of early lymphoid progenitors. *Br. J.*
1207 *Haematol.* **183**, 588–600 (2018).
1208 25. Stehling-Sun, S., Dade, J., Nutt, S. L., DeKoter, R. P. & Camargo, F. D. Regulation of
1209 lymphoid versus myeloid fate 'choice' by the transcription factor Mef2c. *Nat. Immunol.* **10**,
1210 289–296 (2009).
1211 26. Yu, Y. *et al.* Bcl11a is essential for lymphoid development and negatively regulates p53.
1212 *J. Exp. Med.* **209**, 2467–2483 (2012).
1213 27. Schep, A. N., Wu, B., Buenrostro, J. D. & Greenleaf, W. J. chromVAR: inferring
1214 transcription-factor-associated accessibility from single-cell epigenomic data. *Nat.*
1215 *Methods 2017 1410* **14**, 975–978 (2017).
1216 28. Safi, F. *et al.* Concurrent stem- and lineage-affiliated chromatin programs precede
1217 hematopoietic lineage restriction. *Cell Rep.* **39**, 110798 (2022).
1218 29. Lundberg, S. M. & Lee, S. I. A Unified Approach to Interpreting Model Predictions. *Adv.*
1219 *Neural Inf. Process. Syst.* **2017-December**, 4766–4775 (2017).
1220 30. Sekiya, S. & Suzuki, A. Direct conversion of mouse fibroblasts to hepatocyte-like cells by
1221 defined factors. *Nature* **475**, 390–393 (2011).
1222 31. Morris, S. A. *et al.* Dissecting Engineered Cell Types and Enhancing Cell Fate
1223 Conversion via CellNet. 889–902 (2014) doi:10.1016/j.cell.2014.07.021.

1224 32. Wang, H., Yang, Y., Liu, J. & Qian, L. Direct cell reprogramming: approaches,
1225 mechanisms and progress. *Nature Reviews Molecular Cell Biology* vol. 22 410–424
1226 (2021).
1227 33. Treutlein, B. *et al.* Dissecting direct reprogramming from fibroblast to neuron using single-
1228 cell RNA-seq. *Nature* **534**, 391–395 (2016).
1229 34. Cahan, P. *et al.* CellNet: Network biology applied to stem cell engineering. *Cell* **158**, 903–
1230 915 (2014).
1231 35. Kong, W. *et al.* Capybara: A computational tool to measure cell identity and fate
1232 transitions. *Cell Stem Cell* **29**, 635-649.e11 (2022).
1233 36. Kamimoto, K. *et al.* Gene Regulatory Network Reconfiguration in Direct Lineage
1234 Reprogramming (In review). *Stem Cell reports*.
1235 37. Lange, M. *et al.* CellRank for directed single-cell fate mapping. *Nat. Methods 2022 192*
1236 **19**, 159–170 (2022).
1237 38. Liu, Y. *et al.* Increased TEAD4 expression and nuclear localization in colorectal cancer
1238 promote epithelial-mesenchymal transition and metastasis in a YAP-independent
1239 manner. *Oncogene* **35**, 2789–2800 (2016).
1240 39. Khalid, A. B. *et al.* GATA4 regulates mesenchymal stem cells via direct transcriptional
1241 regulation of the WNT signalosome. *Bone* **144**, (2021).
1242 40. Kartha, V. K. *et al.* Functional inference of gene regulation using single-cell multi-omics.
1243 *Cell Genomics* 100166 (2022) doi:10.1016/J.XGEN.2022.100166.
1244 41. Abascal, F. *et al.* Expanded encyclopaedias of DNA elements in the human and mouse
1245 genomes. *Nat. 2020 5837818* **583**, 699–710 (2020).
1246 42. Shi, Y. *et al.* Neural cell adhesion molecule modulates mesenchymal stromal cell
1247 migration via activation of MAPK/ERK signaling. *Exp. Cell Res.* **318**, 2257–2267 (2012).
1248 43. Tsuda, T., Wang, H., Timpl, R. & Chu, M. L. Fibulin-2 expression marks transformed
1249 mesenchymal cells in developing cardiac valves, aortic arch vessels, and coronary
1250 vessels. *Dev. Dyn.* **222**, 89–100 (2001).
1251 44. Stacker, S. A. & Achen, M. G. Emerging Roles for VEGF-D in Human Disease.
1252 *Biomolecules* **8**, (2018).
1253 45. Shi, S. *et al.* Sonic hedgehog promotes endothelial differentiation of bone marrow
1254 mesenchymal stem cells via VEGF-D. *J. Thorac. Dis.* **10**, 5476–5488 (2018).
1255 46. Garattini, E., Fratelli, M. & Terao, M. The mammalian aldehyde oxidase gene family.
1256 *Hum. Genomics* **4**, 119–130 (2009).
1257 47. Wang, R. *et al.* Construction of a cross-species cell landscape at single-cell level. *Nucleic*

1258 *Acids Res.* 2022 (2022) doi:10.1093/NAR/GKAC633.
1259 48. Chen, K. T. *et al.* Liver X receptor α (LXRα/NR1H3) regulates differentiation of
1260 hepatocyte-like cells via reciprocal regulation of HNF4α. *J. Hepatol.* **61**, 1276–1286
1261 (2014).
1262 49. Nobre, A. R. *et al.* ZFP281 drives a mesenchymal-like dormancy program in early
1263 disseminated breast cancer cells that prevents metastatic outgrowth in the lung. *Nat.*
1264 *Cancer 2022* 1–16 (2022) doi:10.1038/s43018-022-00424-8.
1265 50. Gharibeh, L. *et al.* GATA6 is a regulator of sinus node development and heart rhythm.
1266 *Proc. Natl. Acad. Sci. U. S. A.* **118**, e2007322118 (2020).
1267 51. Sato, A. *et al.* C/EBPβ Isoforms Regulate Proliferation and Differentiation of
1268 Regenerating Hematopoietic Stem/Progenitor Cells. *Blood* **134**, 3713 (2019).
1269 52. Harsha Krovi, S. *et al.* Thymic iNKT single cell analyses unmask the common
1270 developmental program of mouse innate T cells. *Nat. Commun. 2020 111* **11**, 1–15
1271 (2020).
1272 53. Horisawa, K. *et al.* The Dynamics of Transcriptional Activation by Hepatic
1273 Reprogramming Factors. *Mol. Cell* **79**, 660-676.e8 (2020).
1274 54. Fidalgo, M. *et al.* Zfp281 Coordinates Opposing Functions of Tet1 and Tet2 in Pluripotent
1275 States. *Cell Stem Cell* **19**, 355–369 (2016).
1276 55. Hahn, S., Jackstadt, R., Siemens, H., Hünten, S. & Hermeking, H. SNAIL and miR-34a
1277 feed-forward regulation of ZNF281/ZBP99 promotes epithelial–mesenchymal transition.
1278 *EMBO J.* **32**, 3079 (2013).
1279 56. Gupta, S., Stamatoyannopoulos, J. A., Bailey, T. L. & Noble, W. S. Quantifying similarity
1280 between motifs. *Genome Biol.* **8**, 1–9 (2007).
1281 57. Wang, Y. *et al.* A permissive chromatin state regulated by ZFP281-AFF3 in controlling the
1282 imprinted Meg3 polycistron. *Nucleic Acids Res.* **45**, 1177–1185 (2017).
1283 58. Ji, W., Mu, Q., Liu, X. Y., Cao, X. C. & Yu, Y. ZNF281-miR-543 Feedback Loop
1284 Regulates Transforming Growth Factor-β-Induced Breast Cancer Metastasis. *Mol. Ther. -*
1285 *Nucleic Acids* **21**, 98–107 (2020).
1286 59. Xu, J., Lamouille, S. & Derynck, R. TGF-beta-induced epithelial to mesenchymal
1287 transition. *Cell Res.* **19**, 156–172 (2009).
1288 60. Schubert, M. *et al.* Perturbation-response genes reveal signaling footprints in cancer
1289 gene expression. *Nat. Commun. 2017 91* **9**, 1–11 (2018).
1290 61. Inman, G. J. *et al.* SB-431542 Is a Potent and Specific Inhibitor of Transforming Growth
1291 Factor-β Superfamily Type I Activin Receptor-Like Kinase (ALK) Receptors ALK4, ALK5,

1292 and ALK7. *Mol. Pharmacol.* **62**, 65–74 (2002).
1293 62. Orge, I. D. *et al.* Phenotype instability of hepatocyte-like cells produced by direct
1294 reprogramming of mesenchymal stromal cells. *Stem Cell Res. Ther.* **11**, 1–15 (2020).
1295 63. Stone, N. R. *et al.* Context-Specific Transcription Factor Functions Regulate Epigenomic
1296 and Transcriptional Dynamics During Cardiac Reprogramming. *Cell Stem Cell* **25**, 87
1297 (2019).
1298 64. Goyal, Y. *et al.* Pre-determined diversity in resistant fates emerges from homogenous
1299 cells after anti-cancer drug treatment. *bioRxiv* 2021.12.08.471833 (2021)
1300 doi:10.1101/2021.12.08.471833.
1301 65. Mold, J. E. *et al.* Clonally heritable gene expression imparts a layer of diversity within cell
1302 types. *bioRxiv* 2022.02.14.480352 (2022) doi:10.1101/2022.02.14.480352.
1303 66. Fennell, K. A. *et al.* Non-genetic determinants of malignant clonal fitness at single-cell
1304 resolution. *Nature* **601**, 125–131 (2022).
1305 67. Cao, J. *et al.* Joint profiling of chromatin accessibility and gene expression in thousands
1306 of single cells. *Science (80-.).* **361**, 1380–1385 (2018).
1307 68. Chen, S., Lake, B. B. & Zhang, K. High-throughput sequencing of the transcriptome and
1308 chromatin accessibility in the same cell. *Nat. Biotechnol. 2019 3712* **37**, 1452–1457
1309 (2019).
1310 69. Zhu, C. *et al.* An ultra high-throughput method for single-cell joint analysis of open
1311 chromatin and transcriptome. *Nat. Struct. Mol. Biol.* **26**, 1063–1070 (2019).
1312 70. Ma, S. *et al.* Chromatin Potential Identified by Shared Single-Cell Profiling of RNA and
1313 Chromatin. *Cell* **183**, 1103-1116.e20 (2020).
1314 71. Liu, H. *et al.* DNA methylation atlas of the mouse brain at single-cell resolution. *Nat. 2021*
1315 *5987879* **598**, 120–128 (2021).
1316 72. Stuart, T. *et al.* Nanobody-tethered transposition allows for multifactorial chromatin
1317 profiling at single-cell resolution. *bioRxiv* 2022.03.08.483436 (2022)
1318 doi:10.1101/2022.03.08.483436.
1319 73. Zorita, E., Cuscó, P. & Filion, G. J. Starcode: sequence clustering based on all-pairs
1320 search. *Bioinformatics* **31**, 1913–1919 (2015).
1321 74. Bond, S. R. & Naus, C. C. RF-Cloning.org: an online tool for the design of restriction-free
1322 cloning projects. *Nucleic Acids Res.* **40**, W209 (2012).
1323 75. JM, G. *et al.* ArchR is a scalable software package for integrative single-cell chromatin
1324 accessibility analysis. *Nat. Genet.* **53**, 403–411 (2021).
1325 76. van Dijk, D. *et al.* Recovering Gene Interactions from Single-Cell Data Using Data

1326 Diffusion. *Cell* **174**, 716-729.e27 (2018).
1327 77. Heinz, S. *et al.* Simple combinations of lineage-determining transcription factors prime
1328 cis-regulatory elements required for macrophage and B cell identities. *Mol. Cell* **38**, 576–
1329 589 (2010).
1330
1331
1332
1333